UNIVERSIDADE FEDERAL DE SANTA CATARINA
CENTRO TECNOLÓGICO DE JOINVILLE
CURSO DE ENGENHARIA AUTOMOTIVA

BRUNO PAES SPRICIGO

3D MAGNETIC STEERING WHEEL ANGLE AND SUSPENSION TRAVEL DETECTION
A novel application of 3D magnetic sensing techniques to increase
vehicle safety decreasing sensor overhead

Joinville, Brazil

2016

BRUNO PAES SPRICIGO

3D MAGNETIC STEERING WHEEL ANGLE AND SUSPENSION TRAVEL DETECTION
A novel application of 3D magnetic sensing techniques to increase
vehicle safety decreasing sensor overhead

Thesis submitted as partial fulfillment of the requirements for the degree of Bachelor in Automotive Engineering of the Federal University of Santa Catarina, Technologic Center of Joinville, Brazil.

Supervisor: Prof. Thiago Antônio Fiorentin, Dr. Eng.

Joinville, Brazil
2016

Bruno Paes Spricigo

3D Magnetic Steering Wheel Angle and Suspension Travel Detection
A novel application of 3D magnetic sensing techniques to increase
vehicle safety decreasing sensor overhead

Work Approved. Joinville, November 28th 2016:

Prof. Thiago Antônio Fiorentin, Dr. Eng.
Supervisor

Prof. Marcos Alves Rabelo, Dr. Eng.
Guest 1

Prof. Antônio Otaviano Dourado, Dr. Eng.
Guest 2

Joinville, Brazil
2016

ACKNOWLEDGMENTS

ABSTRACT

Electronics and control are continuously growing subjects in the automotive industry. The development of new technologies to reduce consumption, increase comfort and handling is the number one priority of many manufactures. Various systems that make nowadays vehicles more secure like TCS (Traction Control System) and ESP (Electronic Stability Program) rely on sensing several variables like individual wheel speed and suspension displacement to compare it to an analytical model and decide if action is needed or not. The main target of this work is to propose a smart use of a new 3D magnetic sensor to improve the quality and precision of the suspension displacement measurement and, because of the greater capabilities of the sensor, detect the steering wheel angle at the same time. The mechanical and magnetic implementations are discussed in detail.

Key-words: smart suspension. magnetic sensor. suspension displacement measurement.

RESUMO

Eletrônica e controle são crescentes tópicos na indústria automotiva. O desenvolvimento de novas tecnologias para reduzir consumo, aumentar conforto e dirigibilidade é uma grande prioridade para muitas empresas. Muitos dos sistemas que fazem os veículos atuais mais seguros como TCS (sistema de controle de tração) e ESP (sistema de controle de estabilidade) dependem da detecção de diversas variáveis, como velocidade individual das rodas e curso da suspensão, para que seus respectivos valores sejam comparados a um modelo analítico para tomar a decisão se há necessidade de ação ou não. O principal objetivo desse trabalho é propor o uso de um novo sensor magnético 3D para aumentar a qualidade e precisão da medição do curso da suspensão e, devido às grandes capacidades do sensor, detectar também o ângulo de direção simultaneamente. As implementações dos sistemas mecânicos e magnéticos serão discutidas em detalhe.

Palavras-chaves: suspensão inteligente. sensor magnético. detecção do curso da suspensão.

LIST OF FIGURES

LIST OF TABLES

LIST OF SYMBOLS

$\vec{B}$ Magnetic field;

$B_\perp$ Perpendicular magnetic field;

B_{amp} Amplitude of magnetic field;

B_{tan} Tangential component of magnetic field;

B_{vert} Vertical component of magnetic field;

B_x Magnetic field in x;

B_y Magnetic field in y;

B_z Magnetic field in z;

Br Remanence magnetic field;

d Displacement of magnet;

D_i Absolute deviation;

$\vec{F}$ Force;

I Current;

K Constant to improve linear results;

l Wheelbase;

O Turning center;

q Electrical charge of the electron;

r Radius;

S_{ang} Calculated value of sensor's angle;

S_{pos} Calculated value of magnet's displacement;

t Thickness;

T Temperature;

$\vec{v}$ Velocity;

V_{cc} IC power supply voltage;

V_H Hall voltage;

V_{in} Input voltage;

V_{output} Output voltage;

w Track of front axis;

β Sensor angle;

δ Average value of steering angle;

δ_i	Steering angle of inner wheel;
δ_o	Steering angle of outer wheel;
Δ	Air gap;
ρ_n	Number of carriers per volume;

CONTENTS

1 INTRODUCTION

The automotive industry invests lots of resources in embedded electronics and control, developing new technologies aiming for fuel consumption reduction, increase of combustion efficiency and improvement of comfort and handling with chassis systems. The safety level of nowadays vehicles is mainly a consequence of the always growing amount of sensors, actuators and controllers inside these vehicles. It is known that increasing driver's assistance with electronics has lead to more safety. The increasing development of autonomous driving vehicles by some manufacturers is a great evidence that using computer to make some decisions and adjustments in a vehicle is a safety increaser feature.

Chassis systems like TCS (Traction Control System) and ESP (Electronic Stability Program) rely on precise sensing to perform efficiently. These assistance systems measure several variables like individual wheel speed, individual suspension displacement, acceleration of vehicle body and steering wheel angle. A comparison between these values and a mathematical model output is made to identify if the driver is loosing control of the vehicle or if some unwanted wheel-spin or wheel-lock occurs. The actuation of these systems is very important, but it also depends on good sensing and robust control algorithms.

Although better and more precise sensors are developed everyday, the automotive industry is very concerned about costs, therefore, a sensor considered the best and most precise would be ideal to make a vehicle more secure and comfortable, but the costs of implementation might not be feasible on regular vehicles, limiting the application to high-end luxury models or more expensive vehicles like transportation trucks or tractors (agricultural machinery in general). Magnetic sensors are already a reality in the automotive industry with several applications like assessing pedals, crankshaft and camshaft positions. Magnetic sensors are an alternative for current measurement systems because of their numerous advantages like small packaging sizes, low production costs, contactless measurement and an excellent robustness against vibrations, temperature, moisture and dirt (LONG...,). Most of the applications of magnetic sensors require a 1D or 2D sensor, but with the introduction of the 3D magnetic Hall sensors, a whole new range of applications can be explored and improvements of the existing systems and applications are also possible.

The suspension is responsible for the comfort and to maintain the tire-ground contact (GENTA; MORELLO, 2009) and the steering system is responsible for changing the vehicle's direction (GENTA; MORELLO, 2009), so it is fair to say that they influence directly the dynamic behavior of a vehicle. Precise measurement of these variables is mandatory to get good results

of the assistance systems. Potentiometers and accelerometers are among the technologies used to measure suspension displacement. As listed by Genta and Morello (2009), there are at least two approaches to use accelerometers: using two of them, one moving with the vehicle body and the other moving with the wheel (the difference between signals is integrated to get the displacement) or using one accelerometer to estimate the acceleration from the body. Steering angle measurement can be made with optical sensors, potentiometers and magnetic systems. The main motivation of this work is to improve the quality of these measurements and, to suggest a more reliable and efficient system that requires only one sensor and one magnet to measure both system's variables simultaneously.

A 3D sensor has the advantage of the third component of magnetic field, making it possible to map more complex movements. To use its full potential of measurement, this work presents a solution to measure two distinct movements keeping the setup simple with only one magnet and sensor. The working principle is: the suspension movement is attached to the magnet, moving it linearly, while the steering movement is connected to the sensor, rotating it. Simulations were performed to find a precise and robust magnetic setup that fulfills both linear and angular movements range requirements. To transform the magnetic field into position measurement, a magnetic map was developed with two equations taking the three components of the magnetic field as input and outputting two positions. These equations were an initial calculation and needed some constant adjustments to get more precise results. A third method to calculate the positions is presented, where the whole spectrum of angles and linear position is mapped and a interpolation is used to create contours of the positions. The interpolation method is more precise than the others because all the systematic errors are included in the data used to map the spectrum.

1.1 Objectives

Main Objective

- Develop a system that, with one 3D sensor and one magnet, is able to read suspension displacement and steering angle simultaneously.

Specific Objectives

- Suggest an automotive application involving the use of a 3D Hall sensor;

- Use magnetic field to determine relative points;

- Improve performance of actual systems by innovating the measurement method.

1.2 Thesis Structure

This work is structured in seven chapters, being the first one the introduction and the last one the conclusion. The second chapter brings the theoretical background to this work, presenting suspension and steering systems of vehicles, as well as magnetic sensors. It contains explanations about suspension systems, its mathematical models, smart suspensions, steering systems and magnetic sensors. The third chapter presents the context of this work with the state of the art in suspension displacement measurement and the main ideas presented of use for magnetic sensor in suspensions and steering systems. The fourth chapter presents the materials used to complete this thesis, like the softwares used, the hardware involved and the technology used to manufacturer the developed mechanism. The fifth chapter shows the development of the calculations, starting from how to calculate the mechanism to convert linear movement into rotation, the development of the parts, the magnetic map needed to translate three components of magnetic field into two distinct movements, and the robot setup. The chapters three to five are the methodology part of this work. The sixth chapter presents the results of the experiment using a robot and their respective errors. Random points were created to simulate a road profile with different suspension displacement and steering angles. The results of positioning of the experiment were compared with the known points and the errors of the experiment are presented. The final chapter has the conclusion and discussion of the results.

2 BACKGROUND

This chapter presents explanations about suspension systems (including smart suspensions) and magnetic sensors. The approach is to answer what is a suspension system, why is it important, how does it work and how it is classified. After understanding the compromises of passive suspensions, it will be easier to understand the advantages of smart suspension systems and how suspension displacement measurement is important.

2.1 Suspension Systems

A vehicle's suspension is the system that connects vehicle's wheels with its body, in case of a unibody[1] vehicle (Figure 1a). If the vehicle is a body-on-frame[2] one (Figure 1b), the suspension system makes the connection between wheels and chassis. In both cases though, the system is responsible for allowing relative movement between ground and, vehicle increasing comfort for passengers or improving vehicle's stability and safety.

Figure 1 – Unibody and chassi vehicle.

(a) Unibody vehicle.

(b) Chassis frame.
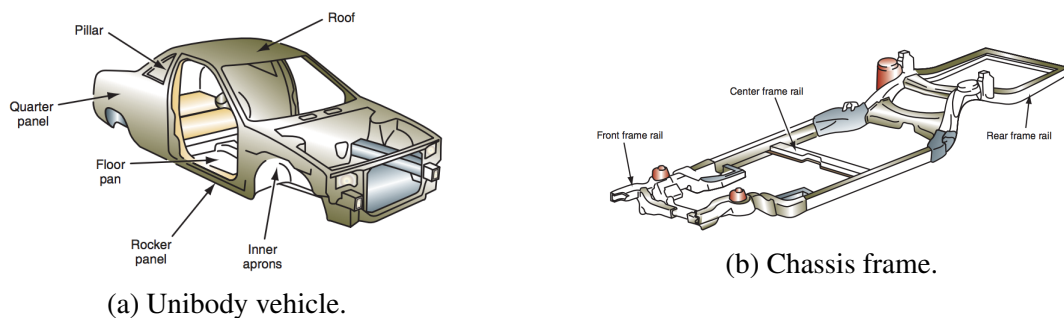
Source: Knowles (2011).

Comfort improvement is achievable because the suspension absorbs and smooths out shocks from road irregularities that would be transfered to the wheel and, furthermore, transmitted to the body as vibrations (GENTA; MORELLO, 2009). Vehicle's stability and safety are obtained by keeping body roll[3] in a level that doesn't compromise the dynamics of movement and maintains a high grip between road and tire under all conditions.

---

[1] Type of body/frame construction in which the body of the vehicle, its floor plan and chassis form a single structure.
[2] Automotive construction method that mounts the body of vehicle to a rigid frame called chassis.
[3] Rotational movement of vehicle body towards the outside of a turn.

According to Genta and Morello (2009, p. 133), a suspension system fulfills its requirements if it:

- Allows a distribution of forces, exchanged by the wheels with ground, complying with design specifications in every load condition;

- Determines the vehicle trim[4] under the action of static and quasi-static forces.

A suspension is mainly composed by two components: an elastic component or spring, and a damper or shock absorber. The spring's main target is to allow relative movement between road and vehicle. The damper's main task is to dissipate this extra energy transfered to the system from road surface variation. The geometry of the linkages[5] is the most used classification mean for suspension systems. These linkages highly affect the efficiency and characteristics of the system because they can either be simple, cheap and deliver average results or extremely complex and expensive, allowing a great number of configuration to improve overall ride quality under many scenarios.

Genta and Morello (2009, p. 134) say that "in theory, tires alone could isolate the vehicle body from forces coming from the road, but their elastic and damping properties are not sufficient to achieve suitable handling and comfort targets, unless at very low speed and on smooth roads.", making suspension systems essential to achieve the adequate amount of handling and comfort. Springs and dampers have a major role in achieving the goals of a vehicle's project because their parameters almost completely define its dynamic behavior.

By transforming relative movement in potential energy, the spring element leaves the static deformation[6] to a different position. It is known that this change of position will result in an oscillatory movement (simple harmonic motion) of the mass connected to the spring, i.e., the vehicle body. Theoretically, in an ideal scenario, this movement would not stop because no energy is lost by the system[7]. Employing a damper or shock absorber is, therefore, mandatory to be able to control this oscillation movement. Essentially, a damper's main task is to take energy out of the system, usually accomplishing it by transforming it in heat, obtaining then a damped oscillatory movement where the amplitude decreases with time.

Simple harmonic and damped motion are very common and, usually, simple to model. In Figure 2, four types of movement are shown in order to illustrate how differently the amplitudes decay with time when varying the damping's coefficient only.

Using a mathematical model named quarter vehicle model (JAZAR, 2009), it is possible to estimate the frequency response of the vehicle, and the suspension behavior can be roughly

---

[4] Trim control is a quasi-static control aiming constant vertical static displacement of the rear axle or of both axles, at any vehicle load (GENTA; MORELLO, 2009, p. 341).

[5] Links connecting the wheels with vehicle's body or frame.

[6] Spring's length at rest when supporting the weight (or part of) of the vehicle.

[7] Considering an ideal system with no friction losses, where all potential energy is repeatedly transformed into kinetic energy and the other way around.

Figure 2 – Dampened Oscillation Movement
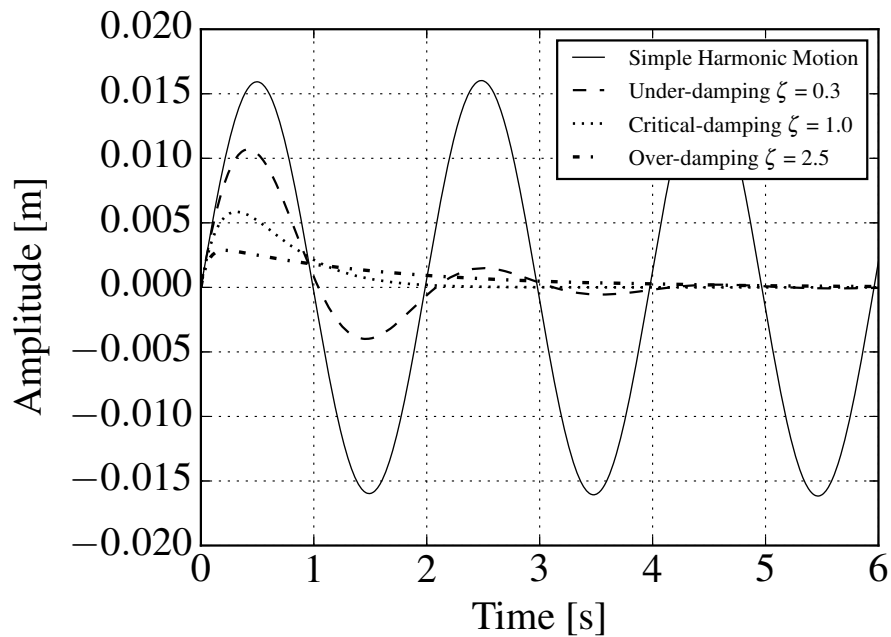
Source: Author, 2016

predicted. Only vertical dynamic behavior can be studied with quarter vehicle model, so horizontal (braking and accelerating dynamics) and lateral studies (handling and dynamics of a vehicle under cornering) are neglected. Nevertheless, the quarter vehicle "[...]contains the most basic features of the real problem and includes a proper representation of the problem of controlling wheel and wheel-body load variations." (JAZAR, 2009). It is also the initial model that is used to begin estimating the spring stiffness and damping coefficient needed to achieve the expected dynamic behavior. This behavior must consider that certain frequencies e.g., the range from 1 to 80 Hz, are more critical because they affect the human body, causing some kind of discomfort (REIMPELL; STOLL; BETZLER, 2001).

A vehicle is a very complex dynamic system that only exhibits vibration in consequence to excitation inputs (GILLESPIE, 1992), thus, its response properties are responsible by the vibration's magnitude and direction affecting the passengers' perception of ride/vehicle as seen in Figure 3.

Figure 3 – Vehicle Perception by Passenger
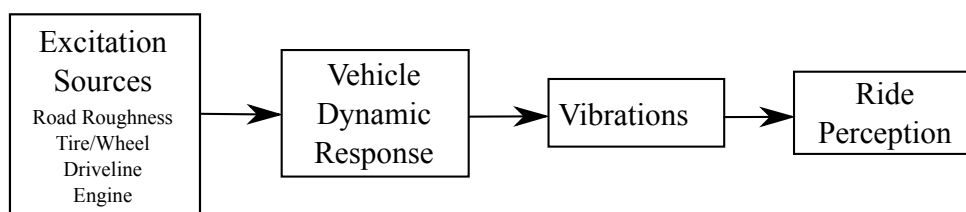
Source: Adapted from Gillespie (1992).

Comfort and active safety are conflicting objectives that suspension systems must fulfill (GENTA; MORELLO, 2009). Suspensions with a high level of comfort should be soft, while to guarantee a constant contact of wheels with the ground they should be rigid (GENTA; MORELLO, 2009). Both these characteristics involve damping coefficient settings, the first requiring small values, while the latter is reachable with higher damping coefficients.

2.2 Smart Suspension

Passive suspension systems[8] can only react to forces coming from the road, because of their nature of only dissipating energy of the system (GENTA; MORELLO, 2009). And because they have fixed values[9] of spring stiffness and damping coefficient, choosing between ride comfort and handling/safety is needed.

> "The limit of these passive suspensions can be easily explained by the impossibility of managing two independent parameters - body vertical accelerations (related to comfort) and vertical force variations (related to active safety) - with a single parameter, the suspension damping coefficient. The two objectives are independent and their optimum values are obtained with different damping coefficients." (GENTA; MORELLO, 2009, p. 340).

Manufactures must then design this parameters according to the target of each project. Sportive cars should be more stable under high cornering or other high demanding situations, therefore, their suspensions should be stiffer, meaning that ride comfort is compromised. Normal cars, in the other hand, should be comfortable and pleasant, but over-improving these characteristics would definitely decrease safety so a balance point is best solution. Sport Utility Vehicles (SUV) and trucks face the same problem, mainly because the wide range of weight they carry requires a wide range of suspension parameters for optimal dynamic behavior under all loads.

Adapting these mechanic parameters is ideal to improve dynamic behavior, but to be able to optimize these parameters adding microelectronics and controllers is recommended. The electronics are responsible to gather and interpret data to know how this parameters should be changed. These are called adaptive, controlled or active suspensions depending on the level of contribution they make (GENTA; MORELLO, 2009).

The most common classification of these systems is:

- Semi-active: Usually is able to adapt its damping coefficient (therefore, adapting to different situations and loads to keep the level of comfort and handling), by measuring suspension displacement, g-force and/or body roll and calculating an according value. There is no addition of energy into the movement (the system is not able to actively change the displacement of suspension), instead it controls how the system will dissipate the extra energy.

---

[8] Systems made only with mechanical parts like springs, dampers and linkages with little or no electronics.

[9] Even though some more advanced systems might have ranges of values instead of a single value, i.e., a gradient behavior, they are optimized for just certain conditions, they cannot adapt.

- Active: The main difference is that adding energy to the movement is possible, therefore, the system can change displacement of the suspension. The suspension sensors measures the kinematic parameters and a controller interprets the data to decide if actuation is needed, if so, it might actuate changing parameters (passive approach), introducing movement to balance displacement (active approach) or both.

In both cases, the system relies on sensors to measure kinematic parameters, a control unit and some actuators. The task of the actuators of a semi-active suspension is to change damper's behavior, what can be done mechanically[10] or electronically[11]. In an active suspension, the actuators are generally more robust because they add energy to the movement using pneumatic, hydraulic or, in same cases, electromagnetic-based systems. Control units might be a specific component for suspension systems or be part of a central unit as the Electronic Control Unit (ECU). Sensing might be simple as a single accelerometer to measure g-force or complex with several sensors monitoring from suspension's displacement to acceleration in different axes of vehicle body.

According to Genta and Morello (2009), the goals of a smart suspension system are trim, roll, damping and/or full active control. Trim control means that the suspension system is able to detect differences in static deformation between the front and rear axes caused by different payloads, maintaining the same ride height at any vehicle load. This allows the vehicle to detect load variation that would completely affect the ride quality and correct it before the movement starts. Roll control is responsible for controlling vehicle roll and roll speed dynamically. Anti-roll bars with static values are used to prevent excessive roll of vehicle body in passive systems. Smart suspensions use sensors to detect movement and interpret the intensity of body roll and decide if action is required, if so, actuators impose an anti-roll bar preload to adapt its performance. Damping control changes damping coefficient of the shock absorber to adapt to various situations, i.e., changing between a sport setup to comfort and vice-versa, dynamically. These controlled dampers are classified as Adaptive or Semi-active:

- Adaptive: The damping coefficient is set to higher levels while in very low or very high (lower than 20 km/h and greater than 120 km/h, respectively) speeds, the first to avoid car bounce while maneuvering and the latter to improve vehicle stability. In between these two situations the value of the damping coefficient is kept low to increase comfort. Even though this is far more range than passive systems, it is not completely adjustable, i.e., hitting a bump while in high speed (high values of damping coefficient) would mean a very uncomfortable ride, the same goes for stability requiring situations while in medium speeds (low damping coefficient);

---

[10] Internal valves inside the damper with variable diameter change fluid's motion.
[11] A damper containing magnetorheological fluid that changes its viscosity according to a magnetic field.

- Semi-active: Based on the Skyhook theory[12], it's more complex but enables more control and improved performance. This system relies on sensing accurately the kinematic parameters to be able to adapt itself to various situations. It calculates the damping force needed to balance the vertical force on suspension using mathematical models with body and wheel speed as input. The system will detect the need of changing damping coefficient and will perform so dynamically, in certain time intervals. It typically includes accelerometers in vehicle body (measuring three axes), a lateral accelerometer on the front of vehicle (or a steering angle sensor), a braking circuit pressure sensor and a car speed sensor.

Full active control fulfill all above objectives in any dynamic situation. It means that for any load or road variation the suspension system can control trim, roll and damping coefficient to keep higher levels of ride comfort and safety. The energy requested by the control system is significant in the third system (damping control) and maximum in the fourth (full active control) (GENTA; MORELLO, 2009).

Smart Suspension systems are strongly dependent on good sensing, because external parameters and resultant movement of vehicle body must be precisely measured in order to provide good actions. Although acting (whether changing damping coefficient or displacement movement) is an important part of the system, precisely sensing and interpreting data is crucial to decide how and when to act.

2.3   Steering System

Depending on how a vehicle's path is controlled, vehicles are classified in two distinct categories, guided and piloted. The first is controlled by a set of kinematic constraints while the later has a guidance system controlled by a human or some kind of device exerting forces that change vehicle's trajectory (GENTA; MORELLO, 2009).

Piloted system is usually composed by a steering mechanism[13], a steering box[14] and a steering column (connecting steering wheel and steering box). The change of direction begins with a rotatory movement of steering wheel that acts on the rack-pinion (or other type of mechanism), shown in Figure 4, generating a linear movement of the steering rack and, therefore, the steering tie rods. The rack moves linearly, pushing or pulling the back (or front) part of the wheel hub producing a rotation around the king-pin axis.

Being responsible for maneuvering and changing vehicle's direction, as well as affecting greatly the dynamic behavior are the main reasons why steering system is among the most

---

[12]   The theory says that it would be ideal to have the vehicle body connected to an inertial reference system, such as the sky, by a shock absorber (GENTA; MORELLO, 2009). It is not feasible, but presents the mathematical model to a setup, in which, the vehicle body would be completely isolated from road variation, body roll and other phenomenon that affect handling and comfort.

[13]   The system of linkages steering the front wheels in a particular way around the king-pin axis, connecting steering arms moving with the suspension stroke to the steering box (GENTA; MORELLO, 2009).

[14]   Transforms steering wheel rotation into a displacement of the steering tie rods or rack (GENTA; MORELLO, 2009).

Figure 4 – Rack-pinion steering box
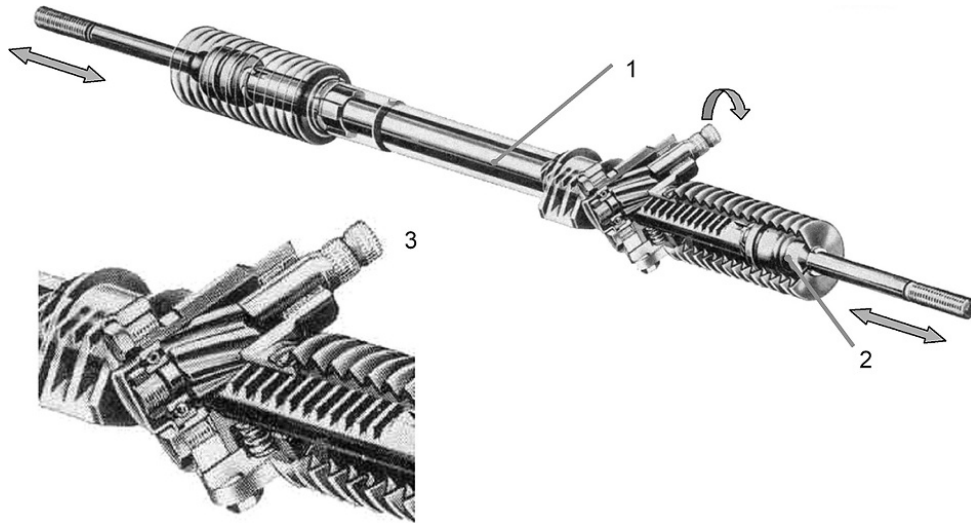
Source: Genta and Morello (2009).

important systems in any vehicle. For modern chassis systems like traction control system (TCS), electronic stability program (ESP) or electronic stability control (ESC), the input of the driver at steering wheel is essential because they mainly focus on predicting some dynamic variables such as speed, intended direction, body roll and others. Theses reference values are extracted from input of various sensors throughout the vehicle and compared to actual values of wheel spin and lateral force to analyze if corrections are needed. A big difference between steering and suspension systems is that assisting systems keep focus on sensing and don't act on steering, with exception of the latest collision avoidance systems that actually change vehicle's trajectory to dodge obstacles.

Low speed or kinematic steering is the definition of a motion of vehicle where the velocity is small enough so the slip of tires are really small and, therefore, there is almost no capability of exerting corner force (GENTA; MORELLO, 2009). Ackerman geometry is defined as the setup of wheel angles where in small speeds the tire slip is zero (JAZAR, 2009). Figure 5 shows the Ackerman geometry where δ_i is the steering angle of the inner wheel while δ_o is the angle of the outer wheel, being δ_i always greater than δ_o because of the difference of radius. This condition is achieved when the projected lines from the rotation axis of all wheels meet in a single point O called turning center.

The distance between steering axes is called track and is represented by w. The distance between rear and front axles is called wheelbase and is represented by l. The Ackerman condition is achieved when:

$$\cot \delta_o - \cot \delta_i = \frac{w}{l} \tag{1}$$

Ackerman is one of the many solutions when designing a steering system geometry, it is ideal for slow speeds and no suspension movement, which, usually, is not the average use of a

Figure 5 – A front-wheel-steering vehicle and the Ackerman condition
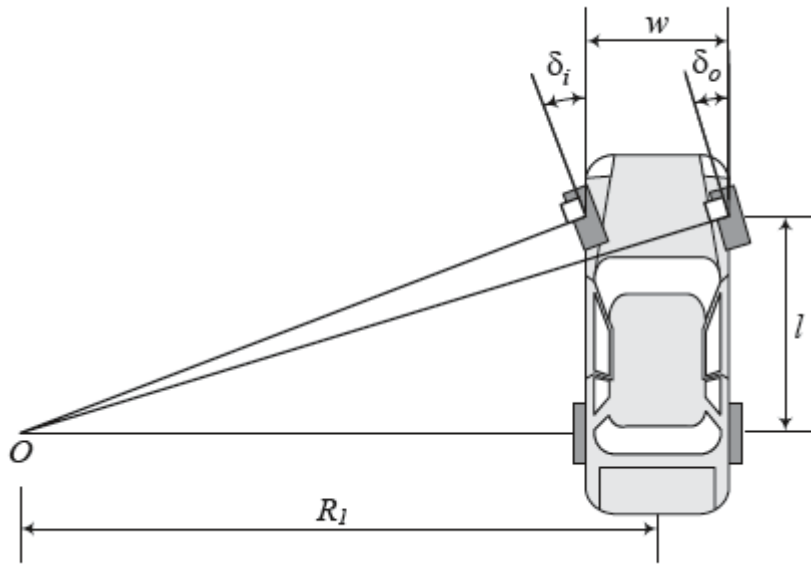
Source: Jazar (2009).

vehicle. There are other geometries with their own advantages and disadvantages, optimized for different situations like race cars employing reverse Ackerman or simpler vehicles with parallel δ_i and δ_o angles. According to Jazar (2009) "there is no four-bar linkage steering mechanism that can provide the Ackerman condition perfectly. However, we may design a multi-bar linkages to work close to the condition and be exact at a few angles." Also, because suspension movement interferes with steering system's angles like camber, caster and toe, the iteration of these two systems must be precisely designed. The initial development of steering system is often made using the bicycle model, in which a 4 wheel based vehicle is transformed into a 2 wheel based one. This model defines δ as the average value of inner and outer steer angles to simplify the further steps of development.

$$\cot \delta = \frac{\cot \delta_o + \cot \delta_i}{2} \tag{2}$$

High speed cornering results in high lateral acceleration which demands high levels of slip angles and Ackerman geometry might not be the ideal solution anymore. Body roll is a major consequence of high speed cornering, it changes normal load in inner and outer wheels and, therefore, their capabilities of exerting corner force. Suspension movement resulted from body roll also interferes with steering parameters making the vehicle handle better or worse depending on the project. Even though steering parameters (angles like caster and camber) may vary because of vehicle movement, they are not adaptive and can not be changed on-the-fly. Meaning that different situations require them to be set and optimized for an intended use while considering all the suspension geometry and movement.

Steering can be a purely mechanic system but in most cases it includes some sort of assistance to decrease the driver's effort and improve comfort. Power steering might be hydraulic or electrical with some configurations having no actual mechanical connection between steering wheel and steering box, the system relies on sensing the driver's input and acting accordingly.

Steering ratio is the angle of rotation of the steering wheel compared to the angle of rotation of wheels (JAZAR, 2009). The average magnitude for street vehicles is around 10:1 (varying widely between models and brands), while other vehicles for different applications like race cars or heavy duty vehicles will, naturally, have different values. Also, some applications use a non-constant value configuration, where vehicles feature a variable ratio steering box, whether applying a variable mechanical rack-and-pinion system or power steering. Steering ratio might vary to increase comfort, safety or aggressiveness for different steering wheel angles, speeds or drive modes.

2.4 Magnetic Position Detection

2.4.1 Hall Sensor

A current-carrying conductive plate crossed by a magnetic field perpendicular to the plane of the plate develops a crossing potential voltage, and this is called Hall Effect. The Lorentz force is the main physical principle of this effect. A moving electron traveling in a magnetic field generates a force shown in Equation 3.

$$\overrightarrow{F} = q\overrightarrow{v} \times \overrightarrow{B} \tag{3}$$

Where $\overrightarrow{F}$ is the resulting force, q is the electrical charge of the electron, $\overrightarrow{v}$ is the velocity of motion and $\overrightarrow{B}$ is the magnetic field. The trajectory of the electron changes because of the resulting force, developing a potential voltage across the plate shown in Equation 4.

$$V_H = \frac{IB_\perp}{\rho_n q t} \tag{4}$$

Where V_H is the Hall Voltage, I is the current passing through the plate, $B_\perp$ is the perpendicular magnetic field, ρ_n is the number of carriers per volume, q is the charge and t is the thickness of the plate. This setup is shown in Figure 6.

The magnetic Hall sensor uses a Hall element to generate the Hall voltage V_H and some electronics to amplify the signal. Some have ratiometric output with $\frac{V_{cc}}{2}$ when there is no magnetic field applied, V_{cc} when a south pole is detected and GND when a north pole is detected (MILANO, 2013).

2.4.2 Position Detection

The detection of a device's position can be done via a magnetic system. A magnet moving attached to the device to be measured with relative motion to a magnetic sensor results in

Figure 6 – Lorentz Force and Hall Effect
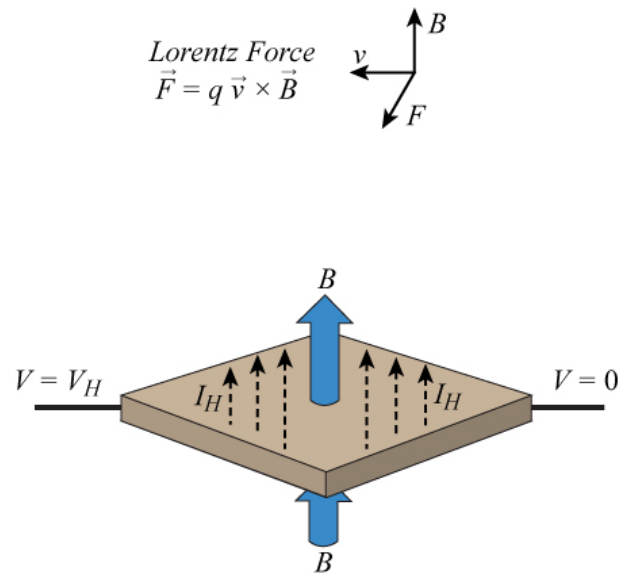
Source: Milano (2013).

a modulation of the magnetic field that is detected by the sensor and translated into mechanical position, orientation or both. A new vehicle can hold up to 80 applications of magnetic sensors like: wheel speed detection, pedals' positions, steering wheel angle, crankshaft and camshaft position, valve position, transmission speed/gear position/actuator, gear stick, oil pump, control elements, window lifter, among others. (TREUTLER, 2001), (HEREMANS, 1997), (RIBEIRO; ORTNER, 2015).

Some advantages of a magnetic position detection system compared to others is:

- Robustness:

  - Contactless measurement and, thus, wear free;

  - Long lifetimes, because modern magnets last up to decades;

  - Perfect for machinery because oil, water, grease and dirt do not influence the magnetic field, so there is no need for airtight seals or other environmental contamination control;

  - Temperature and mechanical pressure are compensated on chip.

- The source (magnet) is mounted on the moving part and does not require cable access;

- High precision, low power requirements, potential for miniaturization;

- Inexpensive to manufacture since the advent of Hall sensors.

One and two dimensional Hall sensors are very common and most of the current applications require only 1D and 2D field detection. The recent introduction of a 3D magnetic

Hall sensor opens the questions for new applications with more complex movements and position detection, for improved old applications and for additional information that can be obtained from the third component of the field.

Modern Hall type sensors are highly linear, which means that the sensor output signals can be directly interpreted as the magnetic field components themselves. These sensors have several embedded digital circuitry for signal processing, most of the time aiming for temperature or pressure compensation or signal amplification. There is also the possibility for on-chip signal processing to give position output directly.

3 CONTEXT

This chapter presents the most common methods used to measure suspension displacement such as potentiometers and accelerometers and ideas to replace these system with magnetic devices. Other types of sensor to measure displacement such as optical devices, capacitive and inductive sensors are not commonly used to measure suspension displacement even though they are well known in industry.

3.1 Suspension Displacement Measurement

There are two main approaches to use accelerometers, the first uses two sensors, one in vehicle body and the other in the wheel. This configuration allows the system to measure the difference in acceleration between unsprung[15] and sprung[16] masses, and by integrating two times the response, the system gets the displacement of the suspension. Another approach involves only one accelerometer in vehicle body and the acquisition of the body acceleration. The acceleration along with the parameters of the suspension components allow the system to estimate the movement of suspension.

Potentiometers can be easily used to measure displacement because of their simplicity and direct correlation between output signal and proportion of movement. There are some linear models, but the most widely used ones have rotational movement. Simple potentiometers have three connectors, a V_{in}, a ground pin (GND) and the V_{output}, where the value of V_{output} varies between $0\ V$ and V_{in} linearly proportional to the range of movement. Some simple mechanical system is then attached to the sensor to convert linear movement from suspension to rotational movement of sensor. The value of V_{output} is translated directly into displacement, therefore this method is simple and reliable.

In semi-active suspension there are two types of action, using a damper made out of ferromagnetic fluid with capability of changing its viscosity when in the presence of magnetic fields and with an electromechanical valves that vary their diameter to change fluid's flow velocity. In active suspension the types of action are usually pneumatic system. The Bose system uses electromagnetic valves with the same type of action of loudspeakers to control suspension movement. Other types of active suspensions with hydraulic systems or other technologies are

---

[15]   The mass of the wheels system and part of the mass of the suspension system, this is the mass directly in contact with the ground.

[16]   The mass of the vehicle that is supported by the suspension system such as vehicle body and occupants.

not widely used. A list of the different makes and their sensing technology is presented in Table 1 and Table 2.

The sensing systems approached by Table 1 and Table 2 are:

- Two accelerometers;

- Potentiometers;

- Magnetic sensors;

- One accelerometer with estimation of displacement.

Table 1 – Semi-active suspension / Mechanical vs. Sensor technology

		Semi Active Suspension	
		Types of action	
		Ferro-fluid / MagneRide	Electro-Mechanical valves
Types of sensor	Accelerometer	No make found.	Ducati; BMW.
	Potentiometer	Audi; Ferrari; Lamborghini; Vauxhall; Cadillac; Buick; Chevrolet; GMC.	BMW; Audi; Ford; Mercedes-Benz; Volkswagen ; Volvo.
	Magnetic Sensor	**No make found.**	**No make found.**
	G-Force based [1]	No make found.	Öhlins-Kawasaki.

[1] Does not actually measure the displacement, gets data from acceleration of vehicle among with other information such as throttle and brake pedals position and steering angle.

Source: Author, 2016.

All companies using ferromagnetic fluid as a mean to vary damping coefficient apply rotational movement potentiometer with some mechanism to transform the linear displacement range into angular measurement. They rely in a ratiometric analog output signal along with a stand-alone ECU that might be integrated with other chassis systems (Delphi Corporation, 2005). Contrarily to magneride, electro-mechanical valves are developed by several companies, therefore automakers can do partnerships or design themselves a specific system to each model or brand as seen in Table 1.

Full active suspensions are not really common in large scale, Mercedes-Benz have their *Magic Body Control* that uses potentiometers to measure the displacement of each suspension together with a stereo camera that scans the road up to 15 m ahead of the vehicle with accuracy of 3 mm in height measurement (Mercedes-Benz, 2013). Other systems of full active suspension either have no data about their sensors or were not implemented in production vehicles, such as the *Bose System*.

Table 2 – Active suspension / Mechanical vs. Sensor technology

		Active Suspension	
		Types of action	
		Full Active Suspension	Full Active Bose Suspension
	Accelerometer	No make found.	No make found.
	Potentiometer	Mercedes-Benz.	No make found.
	Magnetic Sensor	**No make found.**	**No make found.**
Types of sensor	G-Force based	No make found.	No make found.

Source: Author, 2016.

3.2 Suspension Measurement with Magnetic Sensor

A trivial solution to measure suspension displacement with magnetic sensor is shown in Figure 7. A magnet and a magnetic sensor replace the potentiometer, also using the same mechanism to transform linear displacement into angular movement. The angle of the magnet can be measured easily from this approach and, therefore the suspension displacement. This setup also allows any range of displacement because it depends solely on the mechanism.

Figure 7 – Angular measurement with magnet sensor
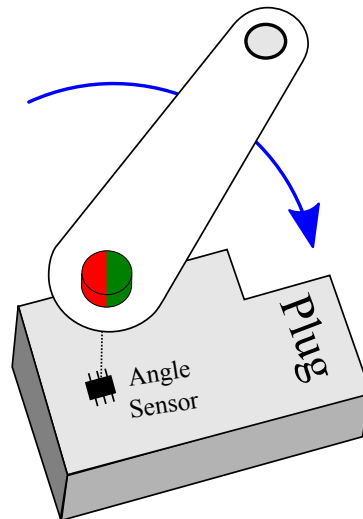
Source: Author, 2016.

Another simple solution consists in a linear position measurement of a magnet that moves along with the suspension by a magnetic sensor. This setup is shown in Figure 8 and in this case, the displacement range depends on the magnetic system so it has to be located where it measures a rate of the suspension movement inside its limits. Because of the arc nature of

the movement, the closer the magnetic system is to vehicle body (attachment point between suspension linkages and vehicle body), the smaller is the amplitude of magnet's movement.

Figure 8 – Linear measurement with magnet sensor
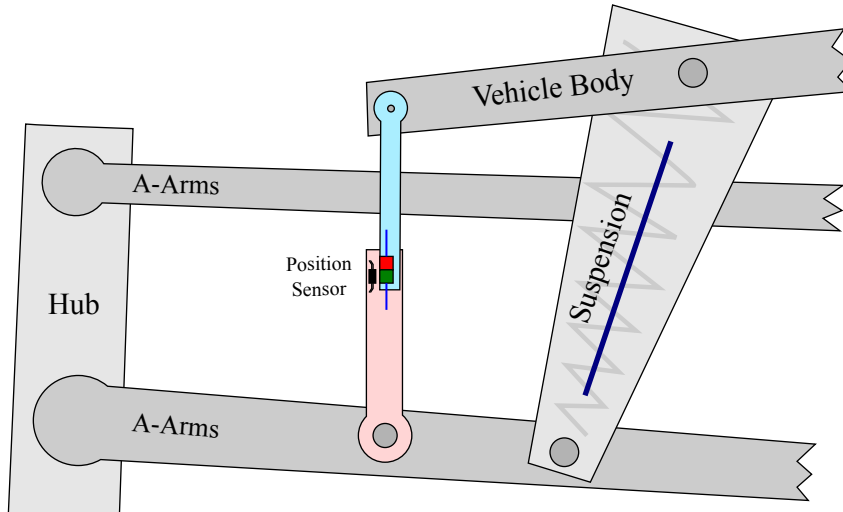
Source: Author, 2016.

Both systems are simple, reliable and would meet the standards to replace other systems in smart suspensions although they are not achieving the full potential of nowadays magnetic sensors, since new sensors have three components of magnetic field and a simple system only uses two of them.

3.2.1 Steering Measurement

Including the measurement of steering angle movement using the same sensor and magnet is an improvement possible because of 3D sensors. These extra components allow a magnet-mechanic coupling that measure more complex movements than strictly linear or angular ones.

An angular input in the steering wheel gives a linear output in the rack, this movement is then again transformed into angular movement of the sensor by a mechanism shown in Figure 9. The suspension movement is acting directly over the magnet, so the magnetic system has to be precisely placed where the full range of the suspension arms is within the limits of measurement of the sensor. A full sketch of the proposed solution to measure both suspension and steering movements with one sensor and one magnet are shown in Figure 10.

Two simple movements generate a complex movement into the central point where the sensor is located. This mechanical setup allows completely isolation from one movement to the other, and even though the magnetic fields are affected by both movements, some magnetic mapping can extract accurately the two(linear and angular) positions out of the three magnetic field components measured by the sensor.

Figure 9 – Linear movement into angular
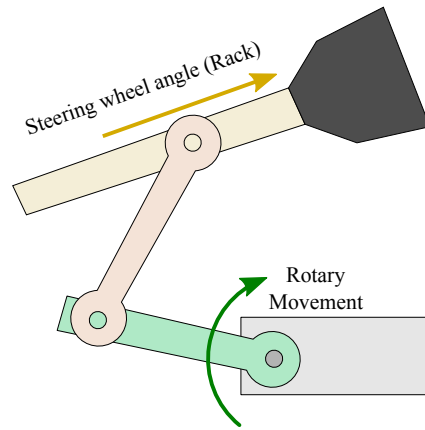
Source: Author, 2016.

Figure 10 – Linear and angular measurements combined
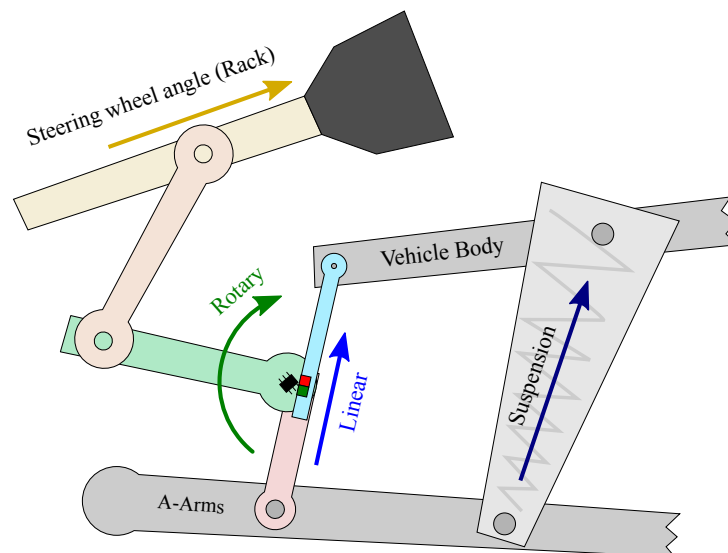
Source: Author, 2016.

4 MATERIALS

This chapter presents all the materials used to develop this work. It covers the majority of the used software, hardware, sensors, magnets, manufacturing methods, etc.

4.1 Softwares

The section of used software consists of all the softwares used to create algorithms, to design the parts, to read the sensor values, and others.

All the algorithms of this work were developed using Python 2.7.11 Anaconda distribution, using the PyCharm Community Edition 2016.1.3 as integrated development environment (IDE). All magnetic simulations were performed using a Python module created by Mr. Dr. Michael Ortner - Researcher from CTR AG that supervised this work. Also, a plotting configuration module was used to improve the graphical quality of the plots in this thesis.

The parts were designed completely using SolidWorks 2016. The whole system was assembled inside SolidWorks and all the movements were simulated generating some videos to illustrate the motion of the proposal. All the printed parts were saved in stereo-lithography (STL) as well as the SolidWorks standard part format.

To organize the bibliography and the several links, blog posts and documents, the software Zotero was used. It creates a bibtex file to be used as the bibliography source for this work.

The illustrations and sketches were drawn using Inkscape 0.91. The motivation to use this software was mainly its open-source nature and the good capabilities of vectorial drawing. Some files were exported as *eps* or *pgf* file format to keep its vectorial nature, allowing text selection in some graphs and no resolution loss when zooming.

Regarding the communication softwares, between robot and computer and between micro controller and computer, all of them were developed by BSc. Marcelo Ribeiro - Researcher from CTR AG that supervised this works. A computer is used as a master in a master-slave communication between the robot controller and a computer. The master computer controls the robot position sending commands to the slave computer that sends information back if the movement was done correctly or not. Velocity and power of the robot may be configurable through the master computer's software. The software is able to get the raw data from the sensor and process it to get the magnetic field. Inside the communication software, a plot with the three components of magnetic field is shown.

4.2 Robot

A robot arm is used to calibrate the system and to move the magnet. The robot is manufactured by Seiko Epson Corporation and the model is the E2C351S and is shown in Figure 11. It has four axes of movement, three with rotational movement and one with translational movement, that allow the robot arm to move in four directions, *i.e.*, x, y, z and u.

Figure 11 – Epson E2C351S
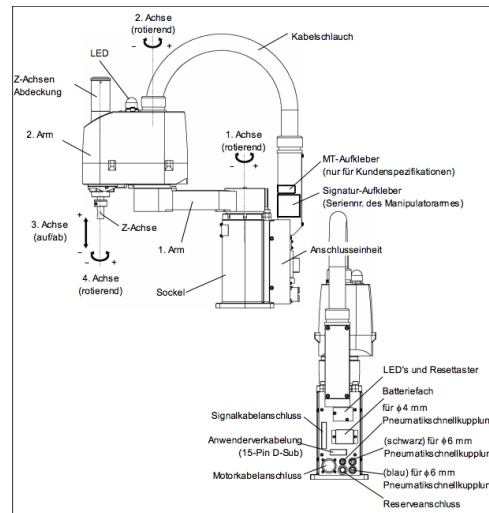
Source: (Seiko Epson Corporation, 2003).

The Annex A shows a table with the specifications of the robot. Among them, the maximum velocity of the axes are: $3600\,mm/s$ for the first axis, $3600\,mm/s$ for the second axis, $1100\,mm/s$ for the third axis and $2600\,deg/s$ for the fourth axis. The maximum precision is: $\pm0,010\,mm$ for the first axis, $\pm0,010\,mm$ for the second axis, $\pm0,010\,mm$ for the third axis and $\pm0,015\,deg$ for the fourth axis. The maximum amplitude is: $\pm110\,deg$ for the first axis, $\pm145\,deg$ for the second axis, $\pm120\,mm$ for the third axis and $\pm360\,deg$ for the fourth axis. The power consumption is $150\,W$ for all servomotors that move the four axes.

4.3 Microcontroller

The microcontroller and the protocol used to read the sensor signal were one Arduino Leonardo board and I^{2}c bus, respectively. The Arduino Leonardo is a microcontroller board based on the ATmega32u4 processor. It has 20 digital input/output pins, a 16 MHz processor, a micro USB connection, a power jack and a reset button (Arduino LLC, 2012). From the 20 i/o pins of the board, the sensor connects to only 4 of them: Ground (GND), V_{cc} of 3.3 V, pin 2 (SDA) and pin 3 (SCL).

The software developed for the microcontroller reads the sensor 12-bit raw values and can deliver as output the raw values of the sensor or the processed values of magnetic field.
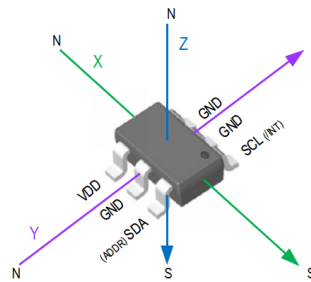
Figure 12 – Arduino Leonardo
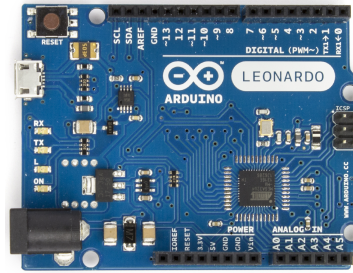
Source: (Arduino LLC, 2012).

4.4 Sensor

The 3D magnetic sensor TLV493D-A1B6 detects the magnetic flux density in three directions; x, y and z as shown in Figure 13.

Figure 13 – Sensor TLV493D-A1B6

Source: (Infineon Technologies Austria AG, 2016).

Among its features are:

- 3D Magnetic sensing;

- Very low power consumption, *i.e.*, $10\,\mu A$ during operations;

- Digital output via 2-wire based standard I^2C interface up to $1\,MBit/s$;

- 12-bit data resolution for each measurement direction;

- B_x, B_y and B_z linear field measurement up to $\pm 130\,mT$;

- Supply voltage range from $2.8\,V$ to $3.5\,V$;

- Working temperature range T_j from $-40°C$ to $125°C$;

- Temperature measurement;

The directions of the axes of measurement are shown in Figure 14.

Figure 14 – Sensor axes of measurement

X-Axis   Y-Axis   Z-Axis
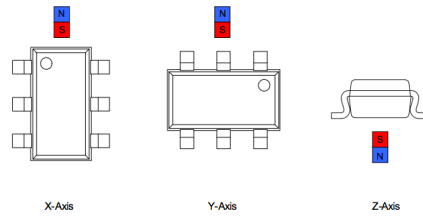
Source: (Infineon Technologies Austria AG, 2016).

4.5 Magnet

Several magnets were considered during the process of this work and after some simulation and test, the chosen magnet to perform the experiments is the 7x7x25mm Y30BH Ferrite Magnet. It is $25\,mm$ long with a square section with $7\,mm$ side. The remanence magnetization field is $Br = 380 \sim 400\,mT$, the coercivity is $bHc = 230 \sim 275\,kA/m$ and the maximum operation temperature is $T_{max} = 250°$.

The ferrite magnet is, usually, produced by powder metallurgical method with chemical composition of $BaO : 6Fe_2O_3$. The ferrite magnets are relatively brittle and hard and special machining techniques should be used in case machining is needed. (ChenYang Technologies GmbH, 2006).

Some other information and physical properties are presented next:

- Good resistance to demagnetization;

- Excellent corrosion resistance;

- Good temperature stability;

- Curie temperature: $450°$;

- Hardness: $480 \sim 580\,Hv$;

- Temperature coefficient of Br: $-0.2\,\frac{\%}{°C}$;

- Temperature coefficient of iHc: $0.3\,\frac{\%}{°C}$;

- Tensile strength: $< 100\,N/mm$;

- Transverse rupture strength: $300\,N/mm$.

More information on the magnet can be found on the Annex B.

4.6   Manufacturing

The 3D printer used to produce the parts for this work is the ProJet 3510 HD*Plus*, manufactured by 3D Systems and presented in Figure 15. It has three printing resolutions, i. e., High definition (HD), Ultra high definition (UHD) and Extreme high definition (XHD). (3D Systems, 2016). The HD resolution has 375 by 375 by 790 dots per inch (dpi) in the x, y and z axis, respectively, and the result is a 32 μm high layer of print. The UHD resolution has 750 by 750 by 890 dpi and 29 μm high layer. The finer resolution, XHD, has 750 by 750 by 1600 dpi and a 16 μm high layer. The accuracy is from 0.025 to 0.05 mm per 25.4 mm in all resolutions.

Figure 15 – ProJet 3510 HD*Plus*

Source: (3D Systems, 2016).

The materials used to print the parts are the VisiJet S300 for the support material and the VisiJet M3 Crystal as the basic material. The properties of the materials are presented in Figure 16.

Figure 16 – Printing Materials Properties

Properties	Condition	VisiJet M3-X	VisiJet M3 Black	VisiJet M3 Crystal	VisiJet M3 Proplast	VisiJet M3 Navy	VisiJet M3 Techplast	VisiJet M3 Procast	VisiJet® S300
Composition		--- UV Curable Plastic ---							Wax Support Material
Color		White	Black	Natural	Natural	Blue	Gray	Dark Blue	White
Bottle Quantity		2 kg	2 kg	2 kg	2 kg	2 kg	2 kg	2 kg	2 kg
Density @ 80 °C (liquid)	ASTM D4164	1.04 g/cm³	1.02 g/cm³	1.02 g/cm³	1.02 g/cm³	1.02 g/cm³	1.02 g/cm³	1.02 g/cm³	N/A
Tensile Strength	ASTM D638	49 MPa	35.2 MPa	42.4 MPa	26.2 MPa	20.5 MPa	22.1 MPa	32 MPa	N/A
Tensile Modulus	ASTM D638	2168 MPa	1594 MPa	1463 MPa	1108 MPa	735 MPa	866 MPa	1724 MPa	N/A
Elongation at Break	ASTM D638	8.3 %	19.7 %	6.83 %	8.97 %	8 %	6.1 %	12.3 %	N/A
Flexural Strength	ASTM D790	65 MPa	44.5 MPa	49 MPa	26.6 MPa	28.1 MPa	28.1 MPa	45 MPa	N/A
Heat Distortion Temperature @ 0.45MPa	ASTM D648	88 °C	57 °C	56 °C	46 °C	46 °C	46 °C	N/A	N/A
Ash Content		N/A	N/A	N/A	0.01 %	0.01 %	0.01 %	0.01 %	N/A
Melting Point		N/A	N/A	N/A	N/A	N/A	N/A	N/A	60 °C
Softening Point		N/A	N/A	N/A	N/A	N/A	N/A	N/A	40 °C
USP Class VI Certified*		No	No	Yes	No	No	No	No	N/A
ProJet Compatibility		SD, HD	SD, HD	SD, HD	SD, HD	SD, HD	SD, HD	HD	SD, HD
Description		ABS-like Plastic	High strength & flexibility plastic	Tough Plastic, Translucent	Plastic, Natural	Plastic, Blue	Plastic, Gray	Castable Plastic	Non-toxic wax material for hands-free melt-away supports

Source: (3D Systems, 2016).

The software used for printing is the 3D Modeler Client Manager also from 3D Systems. The software is used to send the STL files to the printer.

5 DEVELOPMENT

This chapter presents the development of this work. It explains the mathematical analysis, design and production of the mechanism responsible to convert linear movement of steering rack into rotational movement of the sensor, the magnetic system and magnetic mapping used to translate three components of magnetic field into two independent movements and the robot experiments setup.

5.1 Mechanism

Designing the mechanism with feasible dimensions (as if it is going to be applied in a car) was the main target of development. The relation between linear movement and rotational output has to be well known and designed to allow enough angular range of the sensor from the rack displacement. The mathematical analysis and the values considered in the development process are shown in subsection 5.1.1.

5.1.1 Mathematical Analysis

Considering the sensor a fixed point with only rotational movement possible, a Cartesian coordinates system zero can be set on sensor's position, called point A (the final mechanism can be seen in **??**). This crank mechanism is composed of two connection rods, one connected directly to the sensor, or point A, and the other directly to the rack of steering system, or point C, the connection point between these two rods is called point B. The crank mechanism usually converts continuous rotational movement into reciprocating linear movement (or vice-versa), but it can also travel just a part of both movements, like in this application.

Point A has coordinates $(0,0)$ in this system, point C can be assumed to only move in one axis to ease the calculation of point B. Because points A, C and the linear movement of C are not collinear, the approach used to calculate point B coordinates is to find the intersection points of two circles with radius r_1 and r_2, where r_1 is the length of the connection rod between rack and point B and r_2 is the length of the sensor arm connecting the sensor with point B.

Assuming points A and C as the center of the two circles, depending on the position of these two points, there might be zero, one or two points of intersection betweens the two circles. Zero or one points are not useful in this setup because it would mean no actual connection between the two rods or a connection forming a straight line impossible to move because the

force direction and the two rods would be collinear, resulting in an attempt of translational movement instead of rotational.

The two intersection points configuration is shown in Figure 17 with one of the points highlighted as point B. Assuming that C only moves in x axis, its y coordinate, as well as A coordinates are invariable. The yellow line shows the movement of C, generating point C', a new circle that is shown dashed in Figure 17 and, the point B' for the new intersection point. The angle between the sensor arm and y axis of this coordinate system is defined as β and when its value is zero, the sensor axes are completely aligned with the coordinate system. Positive values of β are assumed when point B is in the third quadrant and negative values when B is in the fourth quadrant.

Figure 17 – Two Circles Intersection
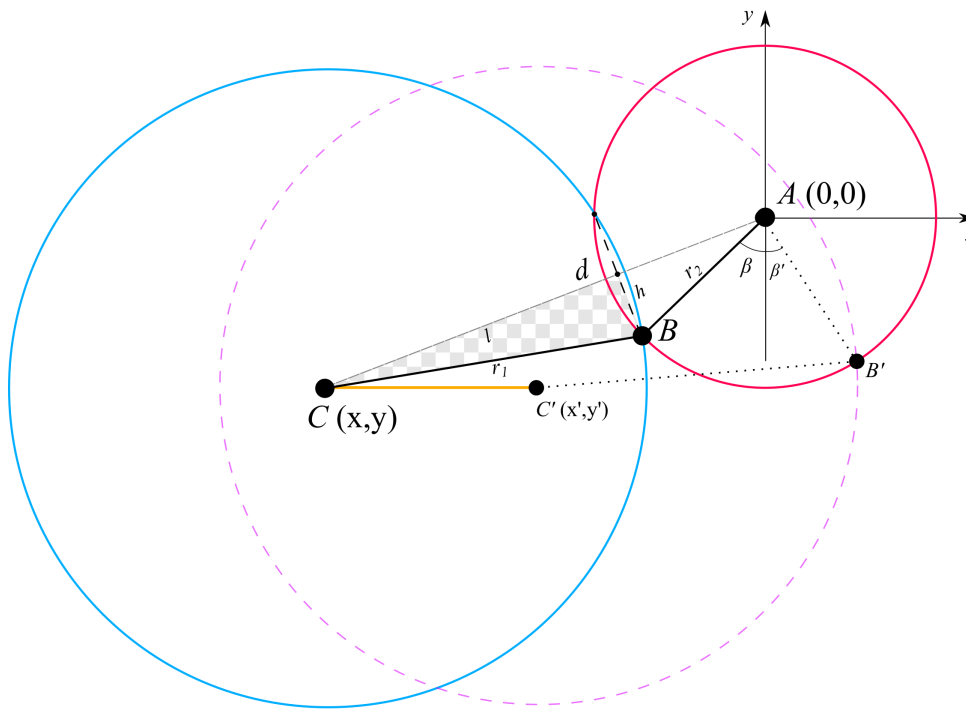
Source: Author, 2016

For this configuration the following can be defined:

$$d = \sqrt{(x_1 - x_2)^2 + (y_1 - y_2)^2} \tag{5}$$

Where d is the distance between points A and C, x_1 and y_1 are the x and y coordinates of point A, respectively and x_2 and y_2 are x and y coordinates of point C.

$$l = \frac{r_1^2 - r_2^2 + d^2}{2d} \tag{6}$$

Where l is the distance from C to the line joining the two points of intersection. They are perpendicular to each other so a small right-angled triangle with legs l and h and hypotenuse

r_1 can be defined. h is then calculated by:

$$h = \sqrt{r_1^2 - l^2} \tag{7}$$

The x and y coordinates of B are then calculated:

$$x = \frac{l}{d}(x_2 - x_1) \pm \frac{h}{d}(y_2 - y_1) + x_1 \tag{8}$$

$$y = \frac{l}{d}(y_2 - y_1) \mp \frac{h}{d}(x_2 - x_1) + y_1 \tag{9}$$

Two coordinates of x and y are presented in Equation 8 and in Equation 9, because there are two points of intersection between two circles. In this case though, only one set of coordinates is important and the lowest point is the chosen to be the connection between the two rods. With the coordinates of point A and B it is possible to calculate the β angle of sensor as seen in Equation 10.

$$\beta = \arctan \frac{x_B}{y_B} \tag{10}$$

The graphical interface shown in Figure 18 is of a calculator developed using Python to verify the range of angular output when varying the position of point C, the length of r_1 and r_2 and the steer movement. It allows a preciser design of the parameters and a better knowledge of the expected output. A larger version of this figure is shown in Appendix A.

Figure 18 – Mechanism calculator
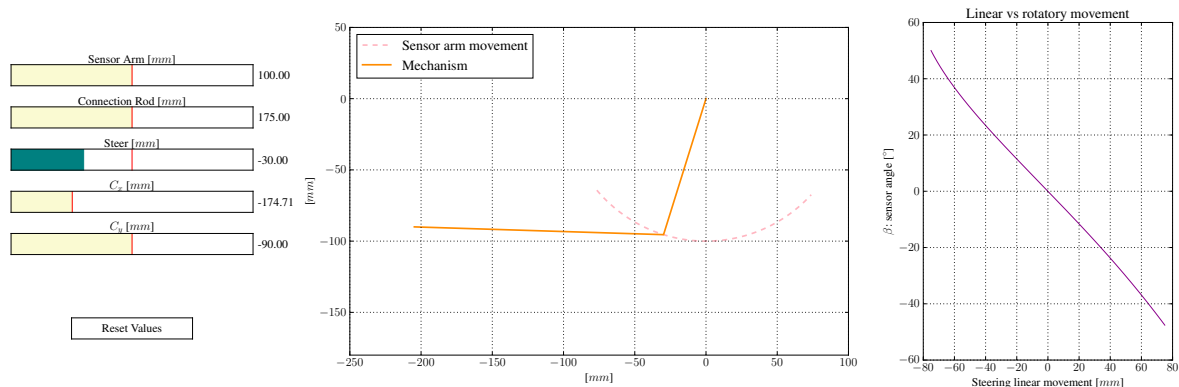
Source: Author, 2016

Through the calculator some parameter values were defined as shown:

- Sensor arm: 100 mm

- Connection rod: 175 mm

- Point C coordinates: [174.71, -90] mm

The value of C_x is more precise because it was adjusted so when the steering wheel is at $0°$, the sensor is also at $0°$. Assuming a range of 150 mm of rack linear travel, the output of the sensor is a range of $97.6°$ varying from $-47.6°$ to $50.0°$, when the steering wheel is completely to the left and right side, respectively. This asymmetry is not a problem because the output angle can be translated to rack linear movement and, with the steering ratio, the steering angle is easily found. So finding the range of β is important to ensure that there is enough range of sensor rotation to map the whole steering wheel positions range. But the mechanism's main function is to find the steering angle using the sensor angle β as input, and it can be done by first calculating point B using Equation 11:

$$B = [-r_1 \sin \beta, -r_1 \cos \beta] \tag{11}$$

Then, the value of linear rack travel can be calculated if point B and the coordinate y of point C are known, through:

$$r_1^2 = (x_B - x_C)^2 + (y_B - y_C)^2 \tag{12}$$

Since r_1, y_B, y_C and x_B are known and invariable, it is easier to create a constant k to group all of this values:

$$-x_C^2 - 2x_C x_B = -x_B^2 + r_1^2 - (y_B - y_C)^2 \tag{13}$$

And then:

$$k = -x_B^2 + r_1^2 - (y_B - y_C)^2 \tag{14}$$

So, applying Equation 14 in Equation 13 and multiplying it by -1 gives:

$$x_C^2 + 2x_C x_B - k = 0 \tag{15}$$

That can be easily solved to find two solutions to x_C, where the smallest is the actual value of the instant rack linear movement, this method needs a previous calculation of point B and an input of the coordinate y of C though. An approach of curve fitting can make this an one-step calculation, therefore reducing the time to translate β into rack movement, while keeping the error below a threshold. Both methods still give the position of the rack as output, which needs to be multiplied by the steering ratio to get steering wheel angle.

$$C(\beta) = 1.6095\beta - 172.60 \tag{16}$$

A first linear approximation is shown in Figure 19 using Equation 16, presenting the comparison between the curve of C as a function of β using the previous approach and a linear fit. The red curve presents the error between the two curves, with a peak of more than two percent when the angle is greater than $-40°$. The R^2 value is 0.9968, which is good for some applications,

but in this experiment (together with some over 2% peaks or error) is not acceptable because this is a systematic error that influences every measurement and result.

Figure 19 – Linear fitting of $C(\beta)$
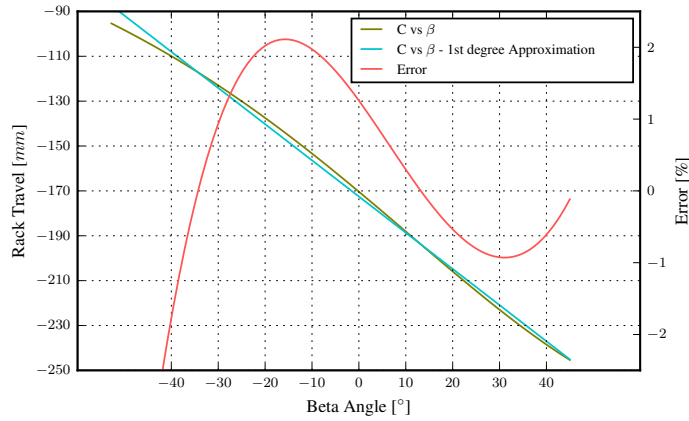
Source: Author, 2016

$$C(\beta) = -8e^{-5}\beta^3 + 2.1e^{-3}\beta^2 + 1.736\beta - 170.67 \tag{17}$$

A third degree polynomial equation can be fitted to the original curve to decrease the error. The Equation 17 is shown in Figure 20 together with the comparison curve and the maximum error, that in this case is slightly smaller than two percent. Even though the maximum error is still big, the average error is not, fluctuating in between -0.3% and 0.3% for most of the values. The R^2 value in this case is 0.9999531.

Figure 20 – 3rd degree polynomial fitting of $C(\beta)$
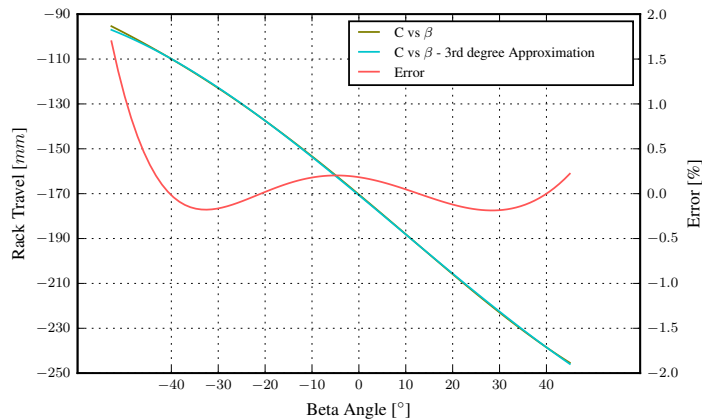
Source: Author, 2016

$$C(\beta) = 6e^{-10}\beta^5 + 7e^{-7}\beta^4 - 9e^{-5}\beta^3 - 3.5e^{-3}\beta^2 + 1.7449\beta - 170.37 \tag{18}$$

Using a fifth degree polynomial fit naturally produces less error values. The Equation 18 is shown in Figure 21 and both curves fit so well that the two lines look one. The R^2 value in this case is greater than 0.9999999. The maximum error is around 0.25% but almost the whole range of angles has almost zero error.

Figure 21 – 5th degree polynomial fitting of $C(\beta)$
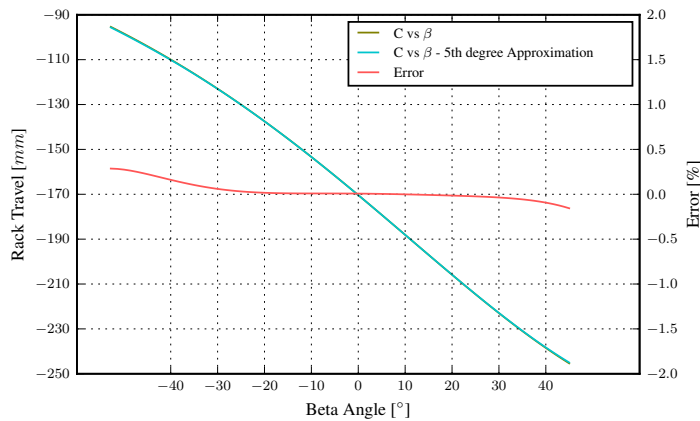
Source: Author, 2016

Increasing the degree of the polynomial fit would continuously decrease the error, but would also increase the processing time. A small test was performed with an algorithm in Python to test the time needed to process different amount of points using the direct method and the equations fitting. Figure 22 shows the amount of time needed for each one of these equations. As expected the behavior when increasing the number of points is linear, the results in Figure 22 are plotted in a *log-log* plot though, because the number of points to process also increased by the power of 10. Results smaller than $10^{-3}\ s$ or $1\ ms$ were not caught by the algorithm, but the plot still shows clearly the ratios between each method.

Figure 22 – Time test for polynomial approximation
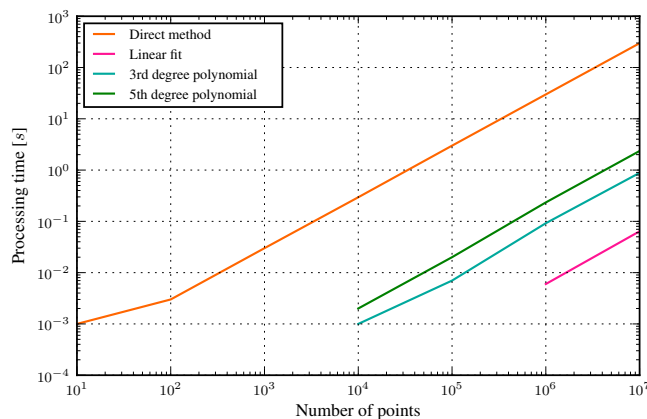
Source: Author, 2016

The ratio between the direct method and the 5th order polynomial (the slowest of the fittings) equation is around 100. This means that some processing time can be saved in this task so it can be used in other parts of the system. But assuming this was the only task to be executed by the system, because of the order of maximum calculating frequencies of theses equations the time of execution is not an issue. Even the direct method has a frequency of 30 kHz in this test, which is a lot bigger than the expected 5.7 kHz of the update rate of the sensor in Fast Mode (Infineon Technologies Austria AG, 2016).

5.1.2 Components Development

The components were designed to be as compact as possible but robust enough to handle all the movements and forces. The first prototype was designed for the robot tests, but using real geometry that could be applied to a car. The mechanism system design consisted of three central parts that hold the Printed Circuit Board (PCB), a magnet holder that is fixed to the robot, a stem connected to the sensor and the system holder.

The PCB layout was defined as a circle of 16 mm of diameter. Two resistors, one capacitor and the sensor are the components of the PCB. It has four connections: VDD (power supply), GND, Serial clock (SCL) and Serial data signal (SDA). Appendix C shows the PCB layout made with the software Eagle and electronic circuit.

The upper part of the magnet holder has a fixed geometry because it is fastened to the robot while the lower part is designed according to the magnet size. It needs to fit the magnet tightly so no relative movement occurs while the robot moves simulating the suspension displacement. A round part is designed to fix the PCB, it has an internal duct for cables and its shape needs to be circular because this is the main rotation part of the system. Figure 23 shows the PCB holder part with its cable channel.

Figure 23 – PCB holder
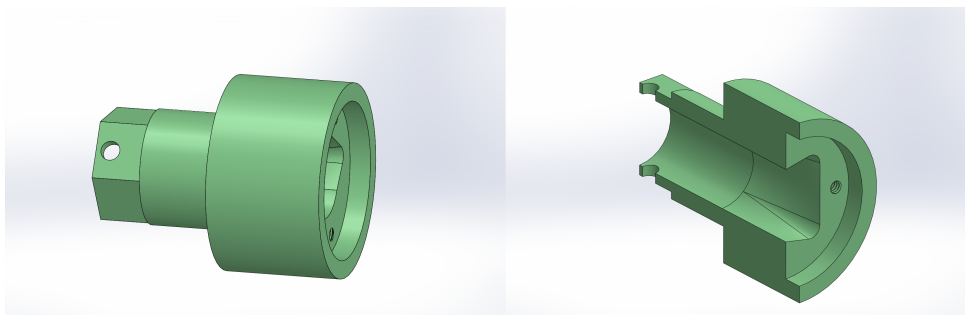
Source: Author, 2016

Two other parts are developed to involve the PCB holder preventing it to make translational movement while it is loose enough to keep friction low so rotational movement is performed easily. One of these parts contains a duct where the magnet holder slides through and

the other part contains the fasteners that keep the system together. Figure 24 shows a cut of the three parts and their final assembly.

Figure 24 – System cut and partial assembly
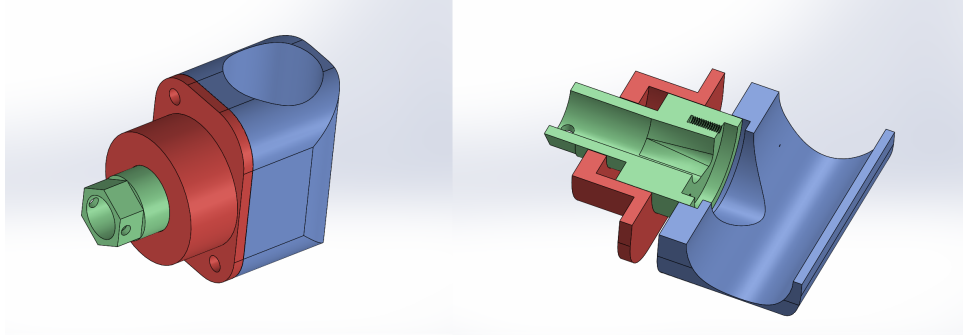
Source: Author, 2016

The sensor arm is a stem with $100\ mm$ between the two connection's centers. It connects with the PCB holder through a hexagonal shaped hole to ensure that every motion of the sensor arm is transfered to the sensor. The final assembly of this part of the mechanism is shown in Figure 25. All components were exported as stereo-lithography (STL) files and printed in order to keep the system light, precise and robust enough.

Figure 25 – Final assembly
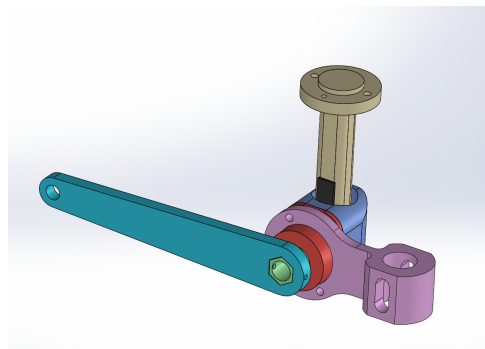
Source: Author, 2016

5.2 Magnetic Map

This section presents the development of the magnetic map with the mathematical analysis to detect linear and angular positions, as well as a combination of these two positions using the magnetic field components.

5.2.1 Mathematical Analysis

State of the art linear position detection requires two components of magnetic field, the tangential component in the direction of the movement and the vertical. Figure 26 shows

the magnetic setup and the simulated x and z components of magnetic field in a linear position measurement.

Figure 26 – Linear position
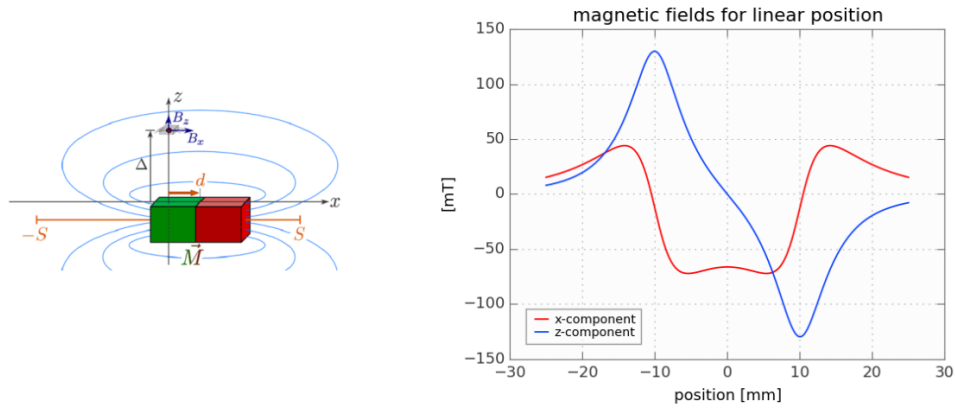
Source: Author, 2016

Because of the dipole field geometry one component will be an even function (x component) of the displacement and the other will be odd (z component). Magnetic position sensing is based on properly choosing the system parameters so the field components are approximately harmonic in a (small) range of d around the origin. The error of this approximation is called intrinsic and depends on the specific setup, i.e. the geometry of the magnet, the stroke S and the air gap Δ. To achieve a linear map between the position d and the sensor output $S_{pos}(d)$ the chip combines the two signals using Equation 19.

$$S_{pos} = \arctan\left(\frac{KB_{vert}}{B_{tan}}\right) - \frac{\pi}{2}sign(B_{tan}) \tag{19}$$

The output of the Equation 19 is typically monotone but not completely linear. The tune of the factor K makes the output more linear inside a range of d slightly smaller than the length of the magnet. An optimal K factor depends on the choice of the magnet, the air gap Δ as well as the length S of the desired stroke. Using the ratio between magnetic fields outperforms systems with only one component because:

- The total amplitude of the field shifts between the two components along the stroke, the combination via `arctan` provides a much larger possible measurement range;

- The system is more stable against variations of Δ because, while the individual components of magnetic field strongly varies with Δ, the ratio between the different components does not.

A simple angular detection magnetic system features a 2D sensor and rotating diametrically magnetized magnet. The rotation center of the magnet and the center of the sensor are

aligned, therefore, the magnetic field is always anti-parallel to the direction of the magnetization and the two transversal components of the sensor can easily determine the angular position using Equation 20.
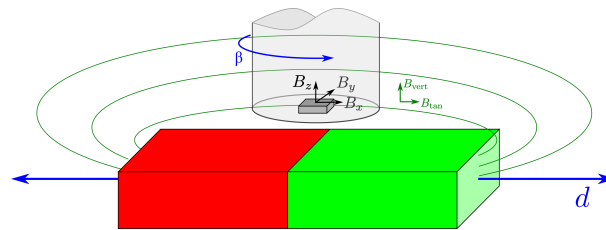
Figure 27 – Angular position
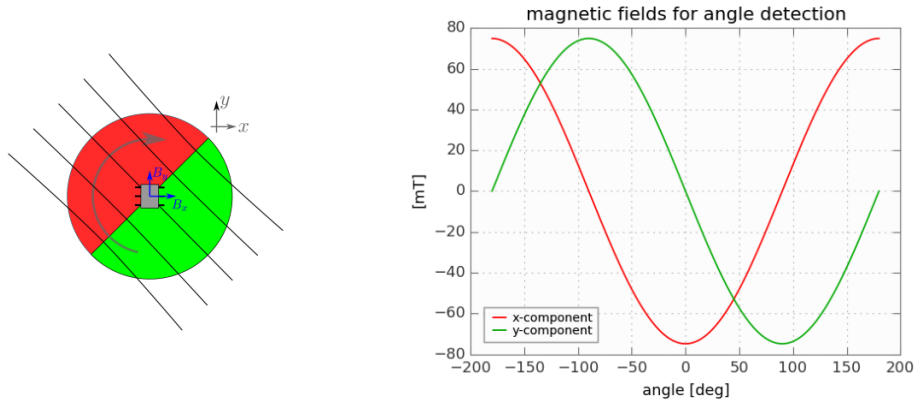
Source: Author, 2016

$$S_{ang} = \arctan\left(\frac{B_x}{B_y}\right) \tag{20}$$

The magnetic setup of an angular position detection system is shown in Figure 27, together with the x and y components of the magnetic field when the magnet rotates from $-180°$ to $180°$. All the $360°$ of rotation are covered by this magnetic map and in case of a small misalignment, a calibration process is needed. The output signal's precision is dependent only of the signal to noise ratio.

Figure 28 – Combination of movements

Source: Author, 2016

Both position detection systems are shown in Figure 28 in the same magnetic setup. The magnet moves in d and its position is calculated using Equation 19. The sensor rotates in β and its value is calculated with Equation 20. The values used by Equation 19 and Equation 20 are calculated by:

$$B_{vert} = B_z \tag{21}$$

$$B_{tan} = \sqrt{B_x^2 + B_y^2} \tag{22}$$

The angle β is the instant angular position of the sensor and is found by:

$$\beta = \arccos \frac{B_x}{B_{tan}} = \arcsin \frac{B_y}{B_{tan}} = \arctan \frac{B_y}{B_x} \tag{23}$$

A combination of all components is calculated by Equation 24 and is named B_{amp}, as shown in Equation 24.

$$B_{amp} = \sqrt{B_x^2 + B_y^2 + B_z^2} \tag{24}$$

5.2.2 Magnetic System

Simulations of the magnetic field were performed to evaluate the magnetic setup. The main variables of the setup are: the magnet dimensions, the air gap Δ and the magnet's magnetic remanence Br. A sweep movement - varying linearly the position from a point to another - of the magnet is simulated with a constant value of sensor angle β. The direction of the magnet's movement is the sensor z axis, moving from $-d$ to d, where d is a value adjusted to deliver the best results of linear and angular position. The results of the simulations are the three components of magnetic field, which are used to calculate B_{vert}, B_{tan} and B_{amp} are then calculated.

Figure 29 – Magnetic field simulation in sensor plane
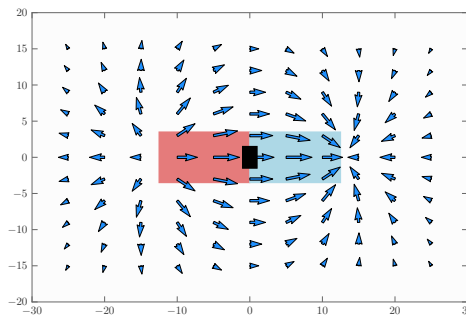
Source: Author, 2016

Figure 29 shows a plane with the vectors of the magnetic field that are Δ distant from the surface of the magnet, this is a two dimension representation of the three dimension vectors of the field. The black rectangle is representing the sensor with $\beta = 0°$, and the red and blue rectangle represents the magnet, where the red side is the north pole and the blue side is the south pole, when $d = 0$. In Figure 29, both parts are perfectly aligned so the magnetic field is symmetric and behaves as expected. But because of building tolerances and construction imperfections, misalignments occur and the magnetic system is not completely symmetric anymore. The three components of magnetic field are shaped accordingly and follow this non-symmetric behavior.

Figure 30 – Magnetic field simulation

(a) Magnetic field simulation

(b) Magnetic field simulation ($45°$)
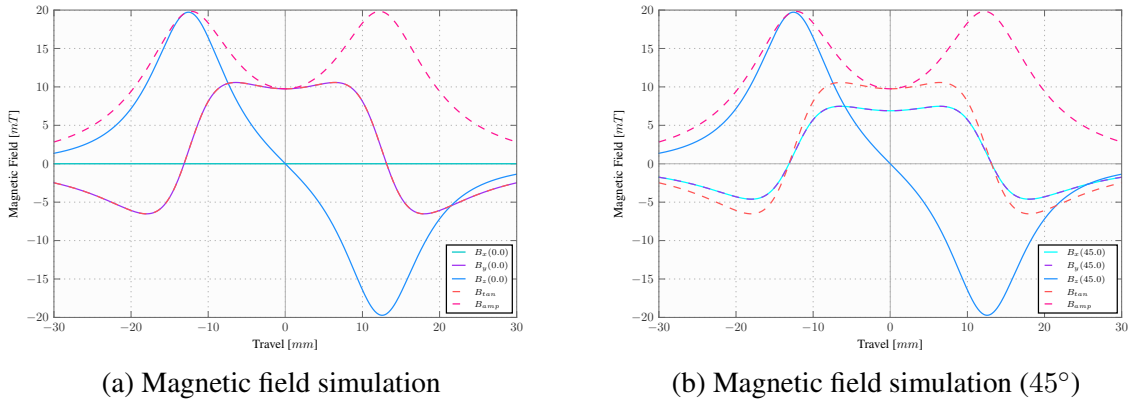
Source: Author, 2016.

Figure 30a shows the components of magnetic field together with the calculated values of B_{tan} and B_{amp}. This scenario occurs when the sensor and magnet are aligned and $\beta = 0°$ and $d = 0$. In Figure 30a all the components are symmetric because this simulation shows the ideal behavior of the system. The B_x component is constant and null because $\beta = 0°$, which is expected since an input of $B_x = 0$ in Equation 20 results in $\beta = 0°$. Figure 30b shows the same magnetic setup of Figure 30a, but with $\beta = 45°$. In this case, B_x and B_y components have the same value as expected. In both cases, B_z, B_{tan} and B_{amp} are the same because these values are not affected by β.

Several cases of building misalignments were simulated to help the calibration process of the system. To predict the behavior or to compare the experimental results, some simulations were performed introducing noise or displacements, this allows a better understanding of the physical system and which components and tolerances are more important.

Figure 31 – Linear position simulation at $\Delta = 2\,mm$
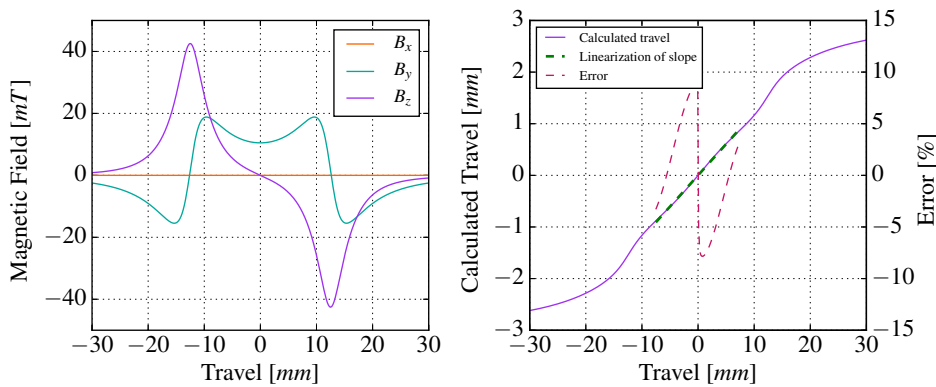
Source: Author, 2016

Results from the simulation show that the linear position measurement through Equation 19 works better if the air gap Δ increases. When Δ is too small, *i.e.*, $\Delta < 2\,mm$, the K

factor of the Equation 19 has less effect and the result is less linear for every case, as shown in Figure 31. The Figure 31 shows the linear position calculation along with a linearization of the output. The maximum error is $12.28\,\%$ and the R value is $R = 0.99919$. The error formula used in this approach divides the absolute deviation D_i by the value of d, as shown in Equation 25.

$$D_i = |x_i - m(X)|;$$
$$Error = \frac{D_i}{x_i} \cdot 100 \tag{25}$$

Where D_i is the absolute deviation, x_i is the calculated travel value d, $m(X)$ is the central tendency (the linearization) and the $Error$ value is the error in [%].

Figure 32 – Linear position simulation at $\Delta = 5\,mm$
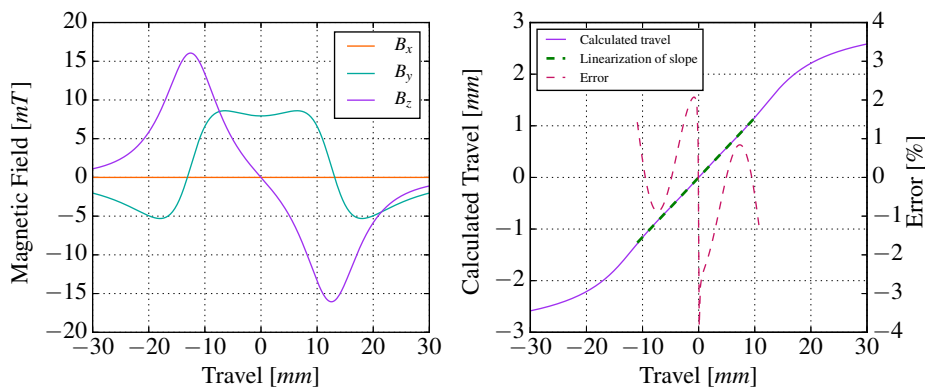
Source: Author, 2016

The opposite case, where $\Delta \geq 2mm$, is easily linearized with the K value, in Figure 32 a simulation with $\Delta = 5\,mm$ is shown. The maximum error is $-3.84\,\%$ and the R value is $R = 0.99994$.

It is also visible the decrease of the maximum value of magnetic field from Figure 31 to Figure 32.

Both results in Figure 31 and Figure 32 should be multiplied by a factor to translate the real values of displacement.

The introduction of small noises in the simulation also influences the result making it less stable. The same simulation with $\Delta = 5\,mm$ with noise inserted is shown in Figure 33. The maximum error peaks over $100\,\%$ and the R value is 0.99941.

The angular position detection through Equation 20 works properly if the system is aligned, but simulations revealed that some parameters influence the precision of the angular position calculation. Misalignments between sensor and magnet can be harmless if they occur in y and z components, but in the sensor's x axis direction any small displacement makes the system really inaccurate, therefore the calculation of the beta angle would only be possible to values of d close to 0.

To improve the precision of the angular measurement two small modifications were proposed in Equation 20: application of a constant value K_{rot} to adjust the curve and make

Figure 33 – Linear position simulation with noise
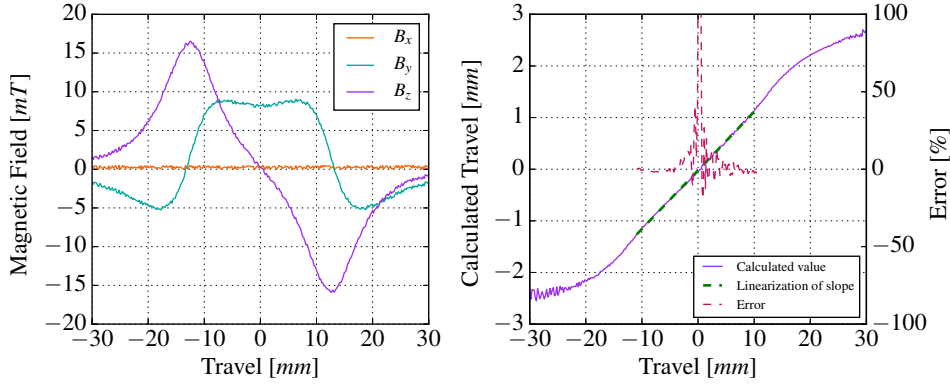
Source: Author, 2016

it more linear or using the linear position result $f(S_{pos})$ as an input. The results of the first approach were still inaccurate. The best solution was to use the linear position result as input in a polynomial equation inside Equation 20 as shown in Equation 26.

$$S_{ang} = \arctan\left(\frac{B_x}{B_y} + f(S_{pos})\right) \qquad (26)$$

Where $f(S_{pos})$ is a polynomial equation in the form $f(S_{pos}) = p_0 S_{pos}^3 + p_1 S_{pos}$. The coefficients p_0 and p_1 are calculated through an algorithm that tests values to find the ones delivering the smallest mean squared error. This approach delivers good results, but is too dependent of the system's calibration. Any movement or vibration requires a new run of the algorithm to optimize the coefficients.

5.2.3 Lookup Table Method

Another method to calculate the values β and d is to use a lookup table. This approach consists of running several sweeps to gather all the values of magnetic field through all the range of linear displacement and angular motion. With these values of magnetic field, the positions d and β are calculated using Equation 19 and Equation 26 for the whole range of d and β. Two two-dimensional arrays were created to store these calculated values of d and β, respectively. This is important because of the measurement's systematic error, for example when measuring $d = -10mm$ and $\beta = 10°$, the results might be slightly different (some close values but not exactly $d = -10mm$ and $\beta = 10°$) because of the misalignments and small noises inserted to simulate the real experiment.

The goal is to create two functions $d_{out}(d, \beta)$ and $\beta_{out}(d, \beta)$ using d and β as input, so two interpolation arrays were created using a 3rd degree spline. Since the spectrum of values is mapped inside d_{out} and β_{out}, it is possible to get the measurement of a point, use Equation 19 and Equation 20 to find d_{calc} and β_{calc} and compare these values to the lookup table to find the

closest values of d_{out} and β_{out}. Also, d_{out} and β_{out} are functions of d and β, so the real values of d and β can be found. The two contour plots are shown in Figure 34.

Figure 34 – Contour Plots for d_{out} and β_{out}
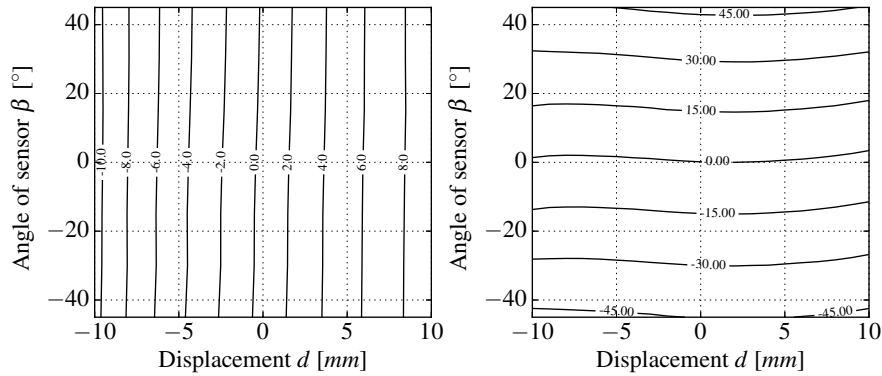
Source: Author, 2016

To find the real value of d and β, the d_{out} and β_{out} arrays are subtracted by d_{calc} and β_{calc}, respectively, so the new arrays d'_{out} and β'_{out} are null for $d'_{out}(d_{calc}, \beta_{calc})$ and $\beta'_{out}(d_{calc}, \beta_{calc})$. Then, another array is created by adding $[d'_{out}]^2 + [\beta'_{out}]^2$. This array has only one null point, exactly for d_{calc} and β_{calc}.

Figure 35 – Contour Plots for $[d'_{out}]^2 + [\beta'_{out}]^2$
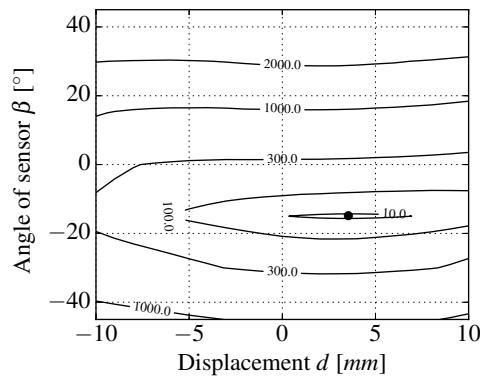
Source: Author, 2016

The black dot comes from a random measurement that returns $d_{calc} = 4\,mm$ and $\beta_{calc} = -15°$, for example. Graphically is possible to get the real values of d and β by getting the x and y value on Figure 35, but for an automated process an algorithm that finds the roots of the array was implemented.

5.3 Robot Tests

The robot adopted to perform the tests has four axes of movement: x, y, z and u, where the first three are translational movement and u is a rotation axis. Although only z is used to

perform the tests, the other axes are needed to calibrate the system. A sketch of the experiment's setup is shown in Figure 36a, and a picture of the final assembly is shown in Figure 36b.

Figure 36 – Robot Experiment

(a) Robot Experiment Sketch


(b) Robot experiment picture
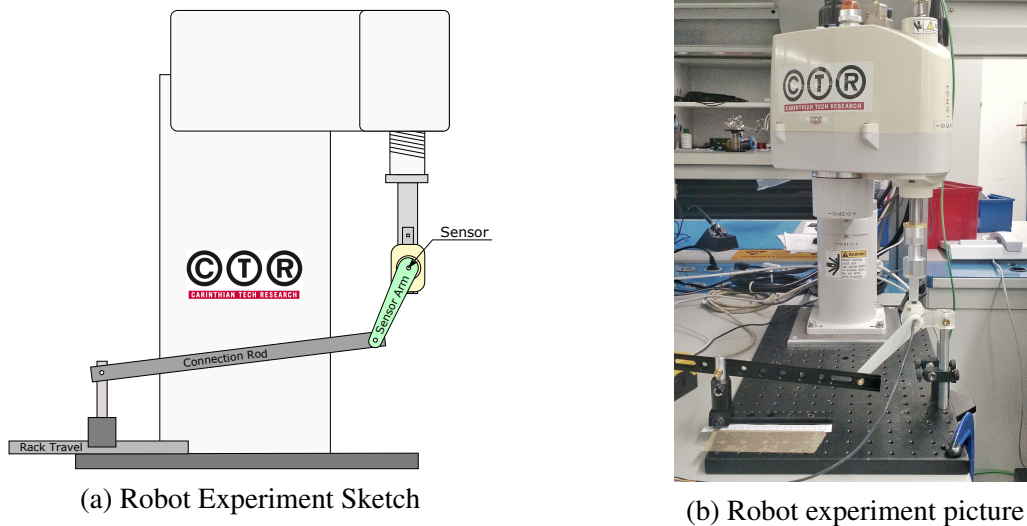
Source: Author, 2016.

Calibrating the system is the first part of the experiment, it is needed to position all four axes in a configuration where the central point of the magnet has no relative x and y positions regarding the central point of the sensor and the surface of the magnet is parallel with the xy plane of the sensor. To accomplish this, several sweeps varying the z position of the robot are performed. Doing an initial sweep, the first coordinate is calibrated. A graphical analysis of the three components of magnetic field reveals the z absolute position of the robot where the value of B_z is zero, therefore, this is the new relative zero z position. The y coordinate of the robot only affects the distance between magnet surface and sensor, so it can be easily adjusted to the desired value without performing any measurement.

The x and u coordinates of the robot affect greatly the B_x and B_y components of magnetic field. This coordinates' calibration involves a trial and error approach. When the sensor arm, and therefore the sensor, is aligned the B_x component of magnetic field, ideally, is a straight line in the x axis of the plot. Any misalignment of robot's x and u will generate a non-constant and, sometimes, non-symmetric curve of the expected B_x component for $\beta = 0$. The robot precision of $0.010\,mm$ or $10\,\mu m$ allows a very precise calibration of all axes, but other important factor to ensure a very tight alignment of the system is the sensor's position. But as precise as the weld to the PCB might be, there will always be some minimal misalignments, meaning that the whole calibration process will not be perfect at the end, either by not giving the expected result when $\beta = 0$ or when β varies. Because the methods to calculate the displacement d or the angle β involve ratios of the different components, the system can handle minor misalignments and errors.

Figure 37 – Robot Experiment Sketch
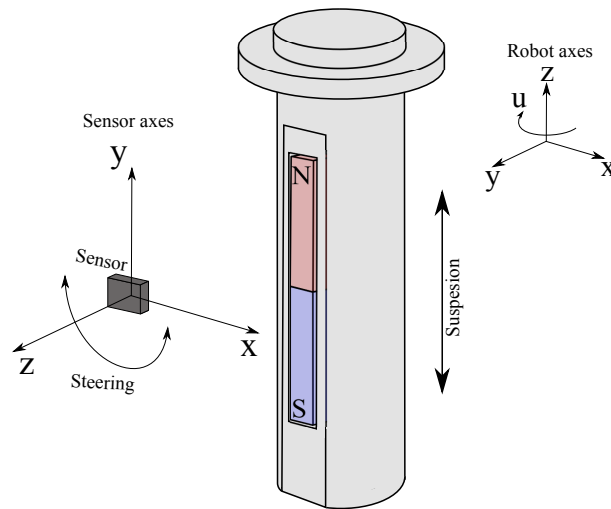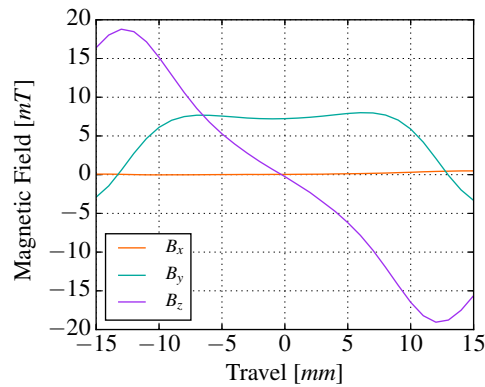

Source: Author, 2016

A sketch of the magnet holder is shown in Figure 37, as well as a magnet representation with its north and south pole. The figure shows the two Cartesian coordinates of the system: the robot's and the sensor's one. The simulated suspension and steering movement are presented right next to the respective moving elements.

After the calibration of the system, a sweep test delivers a result very close to the simulated data. The methodology for the following tests is to generate random points of position d and angle β, where $-10 \leq d \leq 10$ $[mm]$ and $-45 \leq \beta \leq 45$ [°]. The displacement d and angle β are then calculated through the two methods and compared to the reference values.

6 RESULTS

This chapter presents the results from the robot experiments with the magnetic field readings, the linear and angular positions calculation and the comparison with selected random points. These first experiments were performed with a sweep moving the magnet on the z axis of the robot from $-15\,mm$ to $15\,mm$. The air gap value is of $\Delta = 3\,mm$. The results of the magnetic fields B_x, B_y and B_z are shown in Figure 38.

Figure 38 – Initial results of magnetic fields B_x, B_y and B_z

Source: Author, 2016

The results of the magnetic fields B_x, B_y and B_z are shown in Figure 39, along with the calculation of the linear position of the magnet through Equation 19, where the value of K used was $K = 1.06$.

Figure 39 – Magnetic fields B_x, B_y, B_z and the linear position calculation
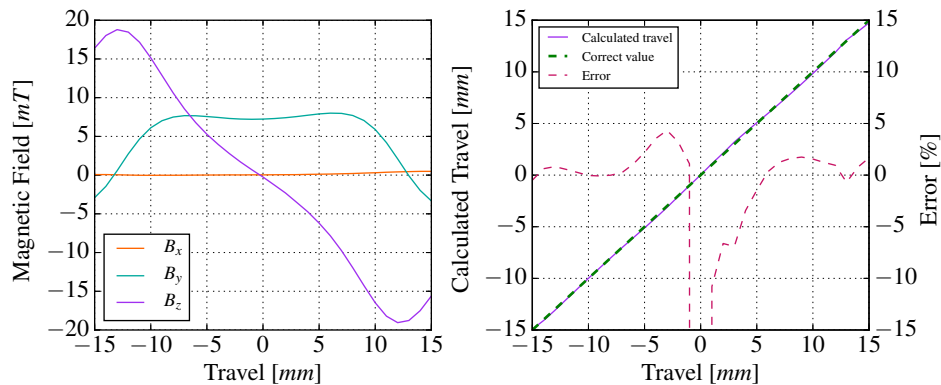
Source: Author, 2016

It is also shown in Figure 39 a line from $(x_1, y_1) = (-15, -15)$ to $(x_2, y_2) = (15, 15)$, which represents the correct values. There is also the error line, with a peak when x is close to 0. The peak happens because, as seen in Equation 25, the absolute deviation D_i is divided by d, so the closer to $d = 0$, higher the error in [%].

The angular position detection, using the Equation 20, is shown in Figure 40 in a test performed with $\beta = 0°$, along with a linearization of the angular calculation result from $-7\,mm$ to $7\,mm$.

Figure 40 – Magnetic fields B_x, B_y, B_z and the angular position calculation for $\beta = 0°$
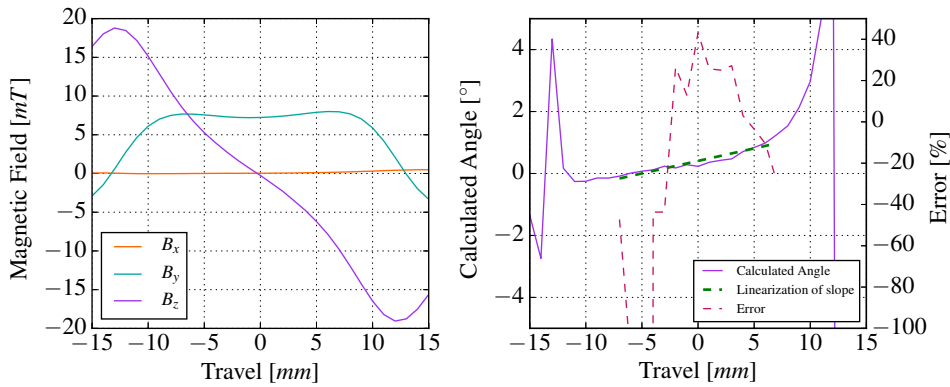
Source: Author, 2016

Because of the setup's misalignments and construction tolerances, the B_x component is not null for the whole displacement d, as expected. So, as seen in Equation 20, if $B_x \neq 0$, the β angle will, naturally, not be zero. The angular position results shown in Figure 40 also have two peaks, located where d is close to the end of the magnet. This happens because at the end of the magnet, $B_y = 0$, so $\frac{B_x}{B_y} \to \pm\infty$. From this point, the results are shown for d from $-10\,mm$ to $10\,mm$, to avoid showing the areas where the angle calculation is inherently inaccurate.

Figure 41 – Magnetic fields B_x, B_y, B_z and the angular position calculation for $\beta = 30°$
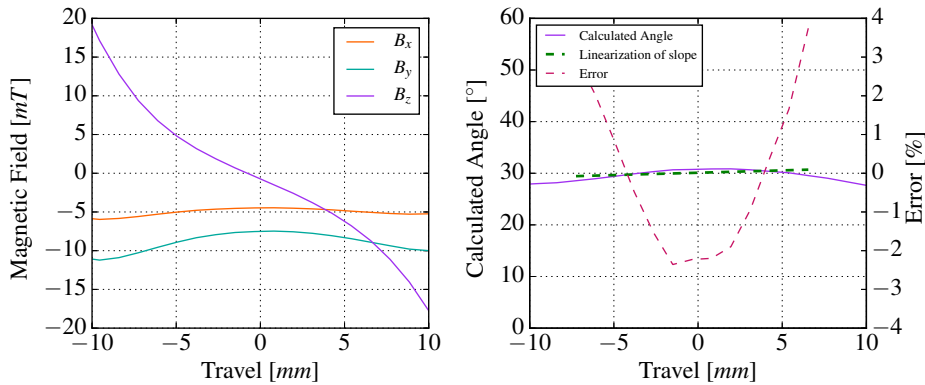
Source: Author, 2016

The angular position detection, using the Equation 20, is shown in Figure 41 in a test performed with $\beta = 30°$. As seen in Figure 41, the results for angular position calculation when

$\beta = 30°$ are significantly better if compared to the ones shown in Figure 40. The percentage error is, naturally, smaller than in the results for $\beta = 0°$ because the absolute deviation D_i is now divided by a greater value. The error value is always under 4%.

Figure 42 – Magnetic fields B_x, B_y, B_z and the angular position calculation for $\beta = -30°$
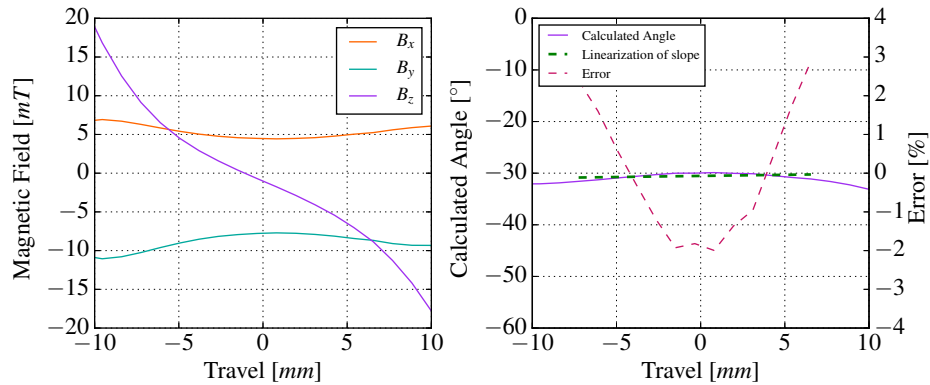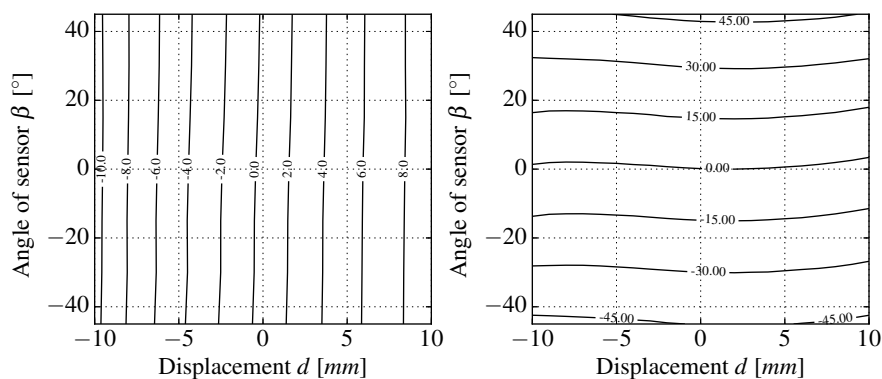

Source: Author, 2016

The results for angular position calculation for $\beta = -30°$ are presented in Figure 42. As in Figure 41, the percentage error is small and the general result is acceptable for this first approach. The error value is always under 3%.

More results of linear and angular position calculation using the equations Equation 19 and Equation 20 are presented on Appendix D.

6.1 Lookup Table Method Application

This section shows the lookup table application to the experiment data. Using the results in Appendix D, two contour plots were made to represent the values of d and β for the spectrum of motion of the experiment, *i.e.*, $-10 \le d \le 10\,mm$ and $-45 \le \beta \le 45°$. Figure 43 shows these two contour plots.

Figure 43 – Lookup contour plots for experiment data

Source: Author, 2016

These contour plots show the result for $d = d_{out}(d_{calc}, \beta_{calc})$ and $\beta = \beta_{out}(d_{calc}, \beta_{calc})$. With the spectrum mapped into the lookup table and into these two contour plots, when a new measurement is done, the calculated outputs of d_{calc} and β_{calc} are compared with the values of d_{out} and β_{out} in Figure 43 to find the real values of d and β.

6.2 Random points analysis

This section presents the random points analysis, where a set of random displacement d points is generated in order to create a road profile. The robot moves the magnet as it was the car suspension going trough this road profile, and the magnetic data is collected. The calculation of d_{calc} through Equation 19 returns a value that is plotted in Figure 44, along with the reference values of the road profile and the percentage error between the real value and the achieved d_{calc}.

Figure 44 – Set of random points for d and β
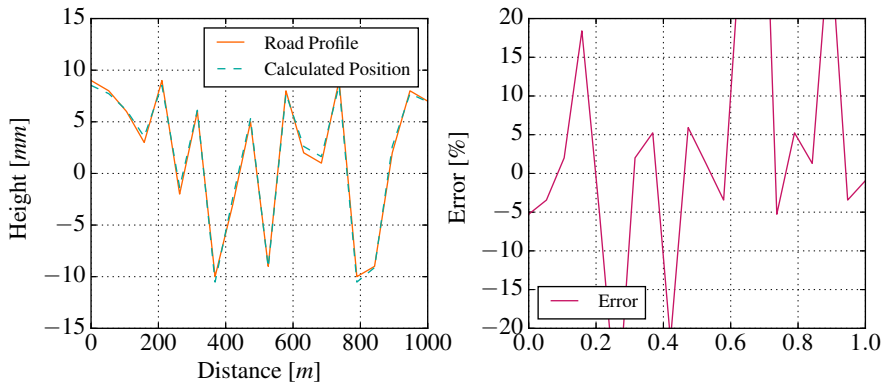
Source: Author, 2016

These experiments are presented for a single steering angle at a time. Figure 44 presents the output for $\beta = -45°$ and Figure 45 presents the output for $\beta = 30°$.

Figure 45 – Set of random points for d and β
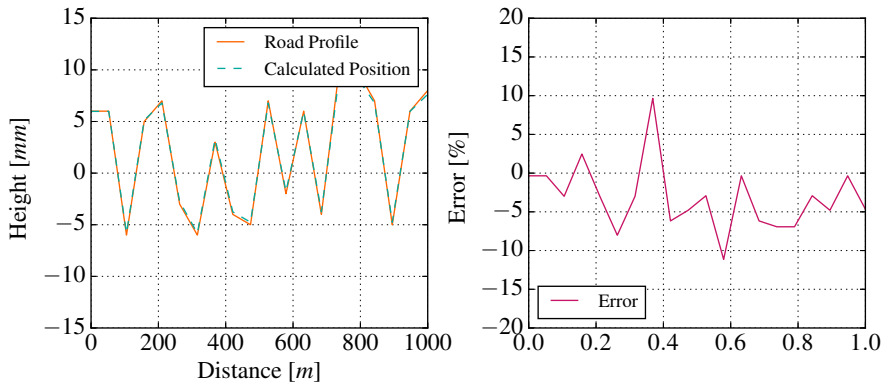
Source: Author, 2016

The other approach, using the lookup table method, is presented in Figure 46. In this case, a parametric curve was created, to vary d and β at the same time, which is closer to reality. So a bi-dimensional array with random values of d and β is created forming a single curve. The experiment was performed for these values and their d_{calc} and β_{calc} values are calculated.

Figure 46 – Set of random points for d and β
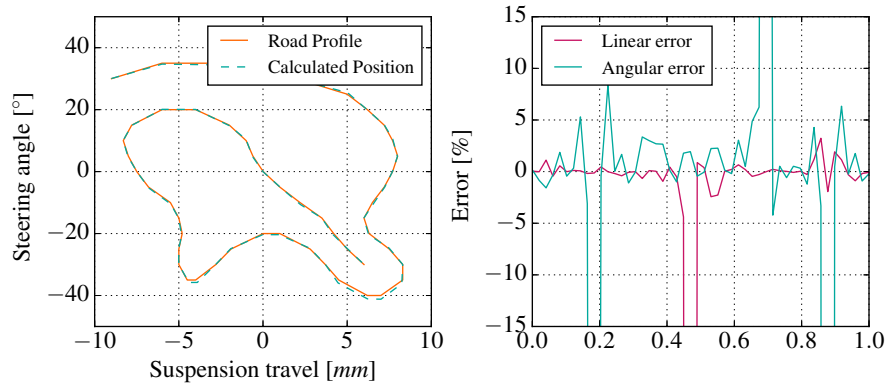
Source: Author, 2016

The parametric curve and the calculated points of d_{calc} and β_{calc} are presented in Figure 46, along with the error in the linear and angular positions calculated data.

6.3 Discussion

A system perfectly aligned delivers the best result with no systematic error, but that is not feasible. Improving the building tolerances of this system is possible because this work developed an initial small prototype, therefore, there are big opportunities of improvement regarding design and manufacturing. Other configurations could be proposed to make the system tighter or the mechanism holder could be designed to attach directly to the robot arm, so there would be no need for calibration of the x and y axes of the robot. The PCB was manually welded, so small misalignments are expected. Although the errors caused by this were minimal, this could be improved by a better method of welding.

The application of this system in a car is the ultimate goal of this project. It would require small changes in the mechanism configuration to allow it to connect to the suspension linkages, but since the system does not suffer any stress while in movement, the parts could also be 3D printed. Another important task of this project goal would be to retrieve the real values of suspension displacement and steering angle. Either because the vehicle does not have these sensors or this data is not easily accessible. In any case, the correct values of displacement and angle are needed to compare with the proposed system and, to calculate the error.

The magnetic map could be improved to get better results from the system. The angular detection is the main issue, becoming highly instable in the region where the tangential

component shows a root. Other important limitation is that the angular range with the current approaches is always smaller than the magnet length.

The angular detection has a high (linear) error behavior for the whole range of movement when a misalignment δ_t is present, and because building tolerances have a feasibility limit, this type of imperfection is always expected. Transversal displacement δ_t and the position of the magnet d are the only variables that affect the error, the β angle has no influence. So it is correct to affirm that $\epsilon = \epsilon(\delta_t, d)$. For small values of δ_t, the error is always of a similar analytical form: $\epsilon(\delta_t, d) \approx \delta_t \cdot \bar{\epsilon}(d)$. It means that if $\bar{\epsilon}(d)$ is known, the error can be easily corrected.

Given that $B_{tan}(x)$ and $B_{vert}(x) \equiv B_z(x)$ and $S_{pos}(x) \equiv x$, three approaches are suggested:

- Scheme 1 - Linear correction: Use the position x to correct the output of S_{ang};

$$S_{ang}^{corr} = \arctan\left(\frac{B_x}{B_y} + P \cdot x\right) \tag{27}$$

- Scheme 2 - Tangent correction: Use the ratio $\frac{B_{vert}}{B_{tan}}$ to correct the error because both have similar shapes;

$$S_{ang}^{corr} = \arctan\left(\frac{B_x}{B_y}\right) + P \cdot \frac{B_{vert}}{B_{tan}} \tag{28}$$

- Scheme 3 - $B_z = B_y$ correction: The error of the y and z components are very similar for small displacements δ_t;

$$S_{ang}^{corr} = \arctan\left(\frac{B_x + P \cdot B_z}{B_y}\right) \tag{29}$$

In all cases, P is a coefficient that must be optimized to each magnetic setup. Figure 47 shows the implementation of the three schemes to calculate the angle. In this simulation the angle $\beta = 0°$, so the expected result is a constant of value 0. The closer the schemes' simulation results are to a 0 valued constant line, smaller the error. This simulation shows very good results regarding the application of theses schemes, specially the third scheme which has a maximum error of $1°$ for the whole range of movement. Applying these schemes is easier than the lookup table because it does not need a map with the whole spectrum of values, the new schemes have an output with smaller errors than the old ones and comparable to the lookup table and the third scheme makes it possible to calculate the angle even further than the tangential components roots, improving greatly the possibilities of different configurations for this system.

Possible further improvements regarding magnetic mapping are:

- Use two parallel magnets to improve transversal stability;

- Develop other schemes that deliver smaller errors and improve stability of the system.

Figure 47 – Angular Range Study
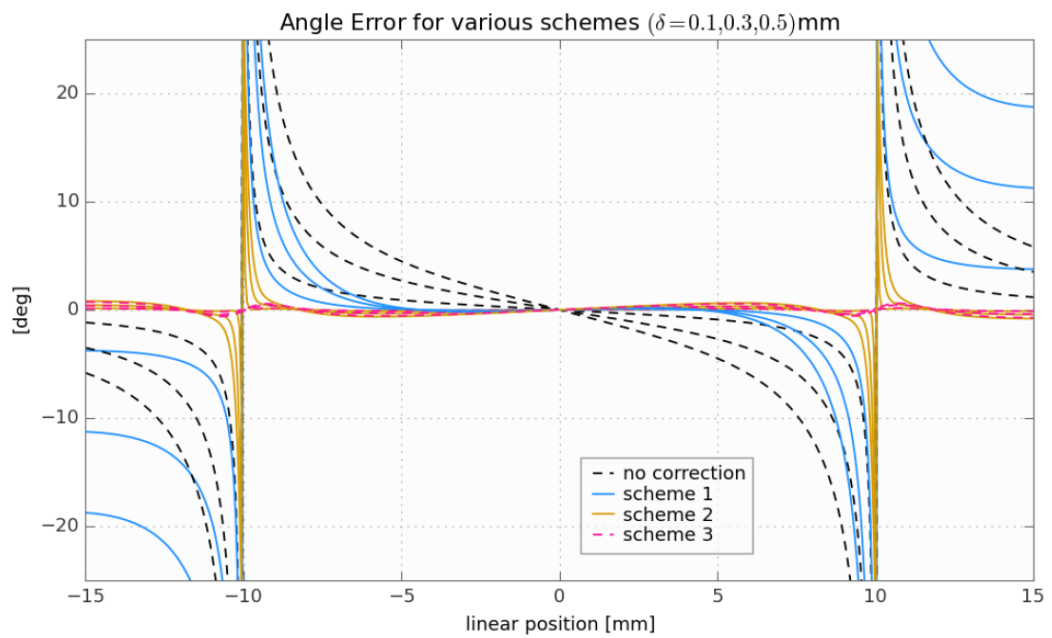
Source: Author, 2016

7 CONCLUSIONS

The main objective of this work was accomplished, the developed system uses only one 3D magnetic sensor and one magnet and is able to detect simulated suspension and steering movements successfully. The specific objectives were also accomplished because a new application involving the 3D Hall sensor is presented, the system was able to use magnetic field to determine relative points and the presented setup uses an innovative method to measure the variables in comparison with actual systems.

Chassis systems and electronic assistance are growing features of vehicles, so is the need of better and more robust sensing systems. The proposal to use only one sensor to measure the combination of suspension displacement and steering angle is feasible. Both systems were simulated in the experiments: the robot moving linearly the magnet to simulate the suspension displacement and the mechanism rotating the sensor to measure steering angle. The initial results with the magnetic formulas demonstrated that the system is capable of identifying the two distinct movements from three magnetic field components.

The precision of the position detection using magnetic formulas is proportional to the building tolerances, as expected. The alignment of the system is crucial to get good results, specially when it comes to the x axis influencing the angular detection. The first approach with the magnetic formulas was successful in detecting the movements, but with no correction of the systematic error the system becomes inaccurate. With the application of constants to adjust the result curves, the error goes down but it is still too high to use in a real vehicle application. The third method of calculation used a spline interpolation with values that included the systematic error, therefore, this approach gives the smallest errors.

The principle of action works, it is possible to combine the measurement of suspension displacement and steering angle in a single sensor. With three components of magnetic field and a proper magnet map, the system can detect easily the positions of this complex movement. Applying the correct method of calculation, that has the smallest possible error, it would be possible to apply the system in a real vehicle and use the data as input for the chassis systems.

7.1 Future Work Proposal

The suggestions for future work can be resumed in three topics:

- Improve mechanical tolerances;

- Change magnetic map approach;

- Application of the system in a vehicle.

BIBLIOGRAPHY

3D Systems. *ProJet 3510 SD Professional 3D Printer*. 2016. Available at: <http://www.3dsystems.com/3d-printers/professional/projet-3500-sd>.

Arduino LLC. *Arduino Board Leonardo*. 2012. Available at: <https://www.arduino.cc/en/Main/ArduinoBoardLeonardo>.

ChenYang Technologies GmbH. *ChenYang Hard Ferrite (Ceramic) Magnets*. 2006. Available at: <http://www.cy-magnetics.com/CY-Mag-HFerrite.pdf>.

Delphi Corporation. *Delphi MagneRide*. 2005. Available at: <http://www.motor-talk.de/forum/aktion/Attachment.html?attachmentId=488981>.

GENTA, G.; MORELLO, L. *The Automotive Chassis. Vol. 1: Components design*. 1. ed. Berlin: Springer, 2009. (Mechanical Engineering Series).

GILLESPIE, T. D. *Fundamentals of vehicle dynamics*. 1. ed. Warrendale: Society of Automotive Engineers, 1992.

HEREMANS, J. P. Magnetic field sensors for magnetic position sensing in automotive applications. *Materials Research Society Proceedings*, Cambridge University Press, New York, USA, v. 475, 1997.

Infineon Technologies Austria AG. *Low Power 3D Magnetic Sensor with I2C Interface*: TLV493D-A1B6 3D Magnetic Sensor. 2016. 23 p.

JAZAR, R. N. *Vehicle dynamics: theory and applications*. 3. ed. New York, NY: Springer, 2009.

KNOWLES, D. *Automotive Suspension and Steering Systems*. 5. ed. New York: Delmar, Cengage learning, 2011. 595 p.

LONG range magnetic field measurement with magnetic sensors. In: IEEE Industrial Automation, Information and Communications Technology (IAICT 2014). Bali, Indonesia: [s.n.].

Mercedes-Benz. *Magic Body Control*. 2013. Available at: <https://www.mercedes-benz.com/en/mercedes-benz/innovation/magic-body-control/>.

MILANO, S. Product Information, *Allegro Hall-Effect Sensor ICs*. 2013. Available at: <http://www.allegromicro.com/en/Design-Center/Technical-Documents/Hall-Effect-Sensor-IC-Publications/Allegro-Hall-Effect-Sensor-ICs.aspx>.

REIMPELL, J.; STOLL, H.; BETZLER, J. W. *The automotive chassis: engineering principles*. 2. ed. Oxford: Butterworth-Heinemann, 2001.

RIBEIRO, M.; ORTNER, M. Magnetic Field Shaping for Improved 1-D Linear Position Measurement. In: *IEEE 9th International Conference on Sensing Technology (ICST 2015)*. Auckland, New Zealand: IEEE, 2015.

Seiko Epson Corporation. *Scara Roboter Manipulator Handbuch: E2C Serie*. 2003. 69 p.
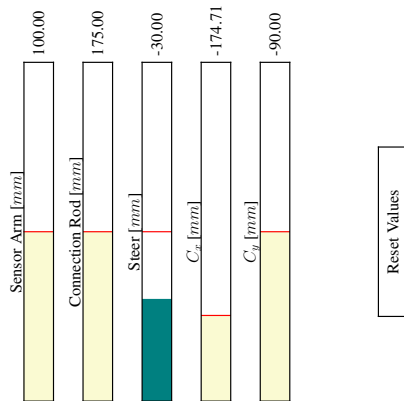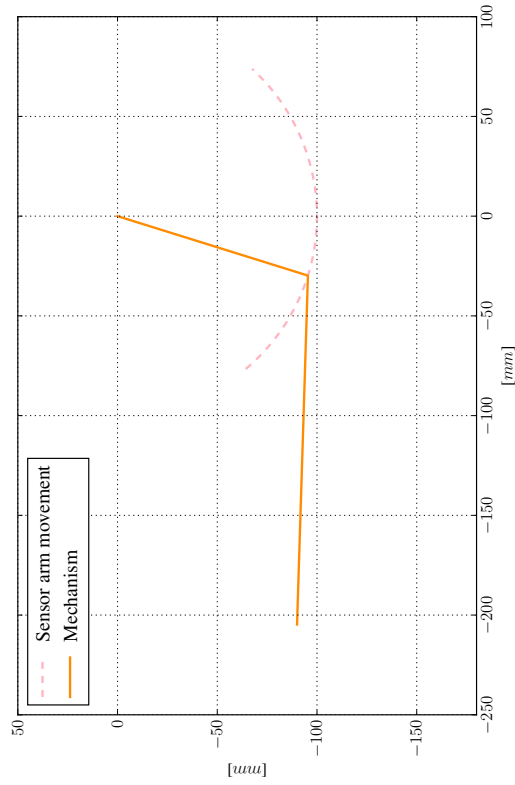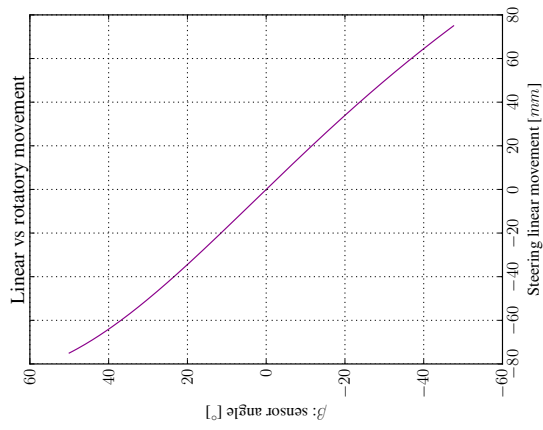
TREUTLER, C. P. O. Magnetic sensors for automotive applications. *Sensors and Actuators A: Physical*, v. 91, n. 1–2, p. 2–6, 2001. Third European Conference on Magnetic Sensors and Actuators.

Appendix

APPENDIX A – MECHANISM CALCULATOR

This appendix presents an image of the Python calculator developed to design the mechanism of this work.

Figure A.1 – Mechanism calculator

Source: Author, 2016

APPENDIX B – PYTHON CODES

This appendix presents some Python codes used in this work. Each section presents a small explanation and the code used.

B.1 Mechanism

This code calculates the B coordinates from A and C coordinates and the sensor arm and connection rod length. It also calculates the β angle for the same setup.

Code B.1 – Python example

```python
1  import numpy as np
2
3  class mechCalculator:
4
5    def __init__(self, a, c, sensorarm, connectionrod):
6      self.A = a
7      self.C = c
8      self.r1 = sensorarm
9      self.r2 = connectionrod
10
11   def calculateB(self):
12     d = np.sqrt((self.A[0] - self.C[0]) ** 2 + (self.A[1] - self.C[1]) ** 2)
13     l = (self.r1 ** 2 - self.r2 ** 2 + d ** 2) / (2 * d)
14     h = np.sqrt(self.r1 ** 2 - l ** 2)
15     self.x1 = (l / d) * (self.C[0] - self.A[0]) + (h / d) * (self.C[1] - self.A[1]) + self.A
           [0]
16     self.x2 = (l / d) * (self.C[0] - self.A[0]) - (h / d) * (self.C[1] - self.A[1]) + self.A
           [0]
17     self.y1 = (l / d) * (self.C[1] - self.A[1]) - (h / d) * (self.C[0] - self.A[0]) + self.A
           [1]
18     self.y2 = (l / d) * (self.C[1] - self.A[1]) + (h / d) * (self.C[0] - self.A[0]) + self.A
           [1]
19
20     return [self.x2, self.y2]
21
22   def calculateBeta(self):
23     B = self.calculateB()
24     if self.x2 >= 0:
25     return np.degrees(np.arctan(abs(self.x2 - self.A[0]) / abs(self.y2 - self.A[1])))
26     else:
27
28     return -np.degrees(np.arctan(abs(self.x2 - self.A[0]) / abs(self.y2 - self.A[1])))
29
30   def calculateB2(self):
31     newCalc = self.calculateB()
32     c1 = self.x2**2 - self.r2**2 + (self.y2 + 90.0)**2
33     pos = -(-2*self.x2 + np.sqrt(4*self.x2**2 - 4*c1)) / 2
```

```
34
35     return pos
```

B.2   Other Python Code

This code calculates the C position when the β angle is given.

Code B.2 – Python example 2

```
 1 import numpy as np
 2
 3 class cposcalc:
 4
 5 def __init__(self, beta):
 6 self.beta = beta
 7
 8 def cpos(self):
 9 if self.beta >= 0:
10 B = [100*np.sin(np.radians(self.beta)), -100*np.cos(np.radians(self.beta))]
11 else:
12 B = [-100*np.sin(np.radians(-self.beta)), -100*np.cos(np.radians(-self.beta))]
13 c1 = B[0]**2 - 175**2 + (B[1] + 60.0)**2
14 pos = -(-2*B[0] + np.sqrt(4*B[0]**2 - 4*c1)) / 2
15
16 return pos
```

B.3   Robot experiment output read and plot

This code is used to read the files with results from the robot experiment. The text files are read and put into variables and plotted. The figure containing the plot is saved as EPS.

Code B.3 – Python example

```
 1 # ---------- Import ----------
 2 from plotConfig_v15BrunoAx1 import *
 3
 4 # ---------- Data Read ----------
 5 dat1 = genfromtxt('filename.txt',delimiter=',',skip_header=0,skip_footer=0)
 6 dat1 = dat1[:,5:8]
 7 dat1 = array([average(dat1[100*i:100*(i+1)],axis=0) for i in range(len(dat1)/100)])
 8
 9 Bx = dat1[:,0]
10 By = dat1[:,1]
11 Bz = dat1[:,2]
12
13 # ---------- Plot ----------
14 xs = linspace(-15,15,len(Bx))
15
16 ax1.plot(xs,Bx,color=ORANGE,label=r'$B_x$')
17 ax1.plot(xs,By,color=TEAL,label=r'$B_y$')
18 ax1.plot(xs,Bz,color=PURPLE,label=r'$B_z$')
19 ax1.grid(True)
20 ax1.set_xlabel(r'Travel [$mm$]')
21 ax1.set_ylabel(r'Magnetic Field [$mT$]')
22 ax1.legend(loc=4,prop={'size':14})
```

```
23
24 # ---------- Save Plot ----------
25 plt.savefig('/Directory/filename.eps', format='eps', dpi=100)
26 plotstyle()
27 plt.show()
```

APPENDIX C – PCB LAYOUT AND ELECTRONIC COMPONENTS

This appendix presents the physical PCB layout made with the software EAGLE. Figure C.1 shows the physical connections and Figure C.2 presents the sensor circuit with the obligatory components.

Figure C.1 – PCB Layout
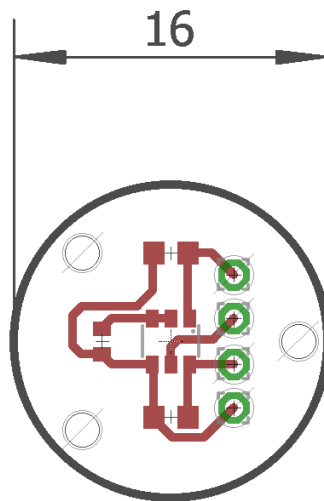
Source: Author, 2016

Figure C.2 – Sensor Circuit
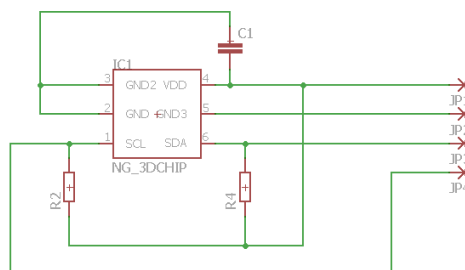
Source: Author, 2016

APPENDIX D – RESULTS OF LINEAR AND ANGULAR POSITION CALCULATIONS

This appendix presents all the results for the magnetic field and the linear and angular positions calculation. As stated in chapter 6, the d range in this results is from $-10\,mm$ to $10\,mm$, to avoid showing the range where the calculation is inaccurate. The results will be presented in two sections, where the first shows the linear position calculation results in seven scenarios, *i.e.*, $\beta = [-45, -30, -15, 0, 15, 30, 45]°$ and the second section shows the angular position detection for the same scenarios.

D.1 Linear position calculation

Figure D.1 – Magnetic fields B_x, B_y, B_z and the linear position calculation for $\beta = -45°$
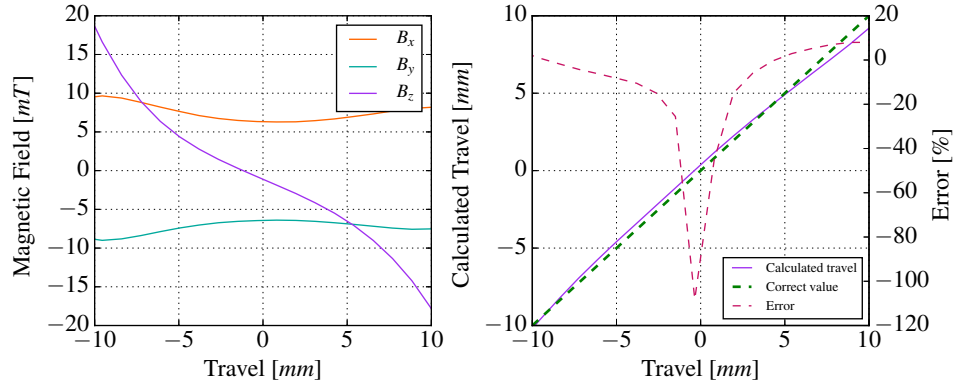
Source: Author, 2016

Figure D.2 – Magnetic fields B_x, B_y, B_z and the linear position calculation for $\beta = -30°$
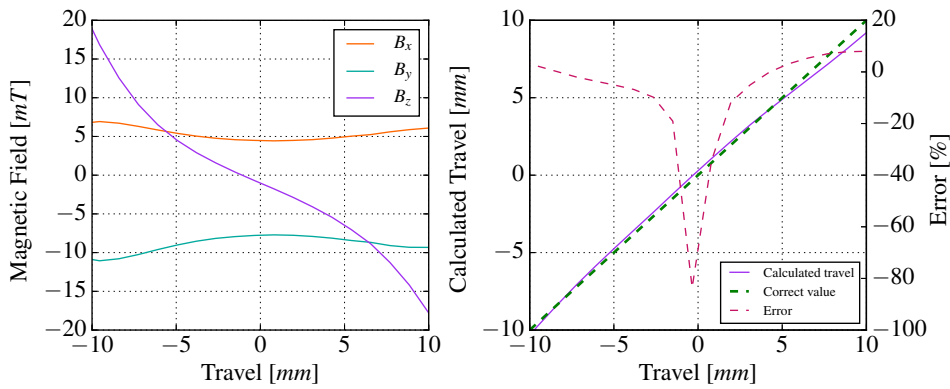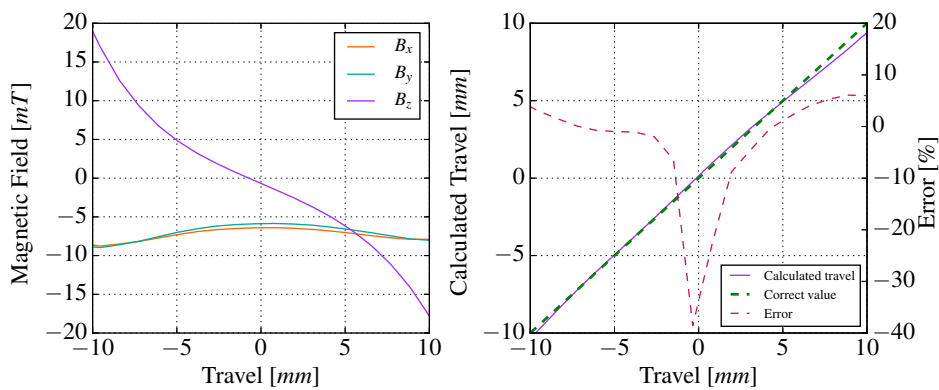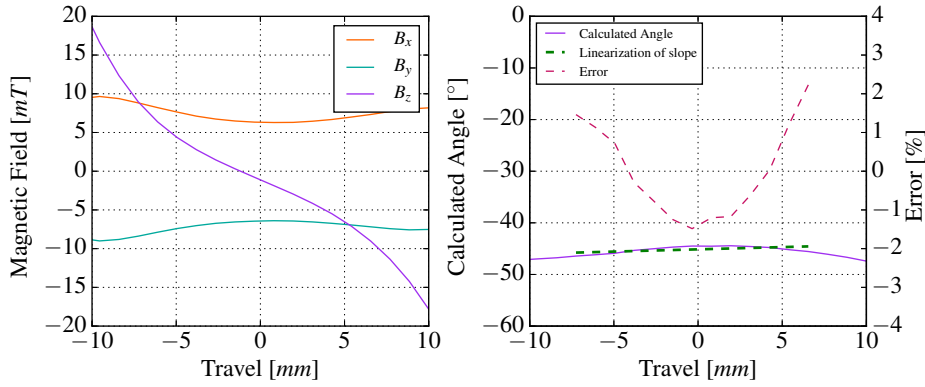

Source: Author, 2016

Figure D.3 – Magnetic fields B_x, B_y, B_z and the linear position calculation for $\beta = -15°$
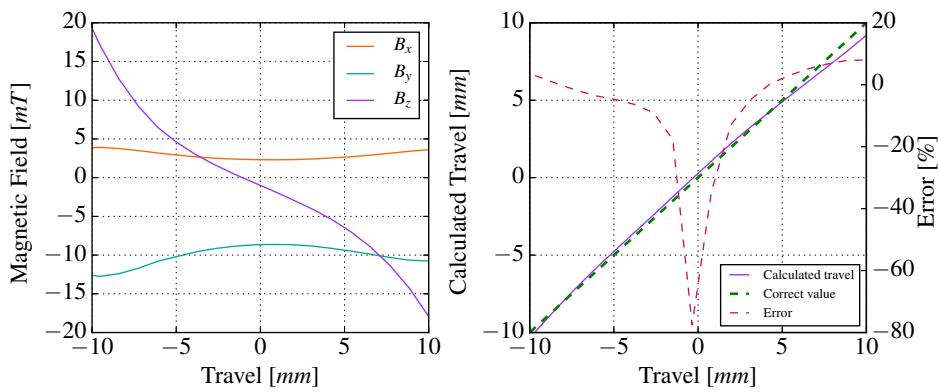
Source: Author, 2016
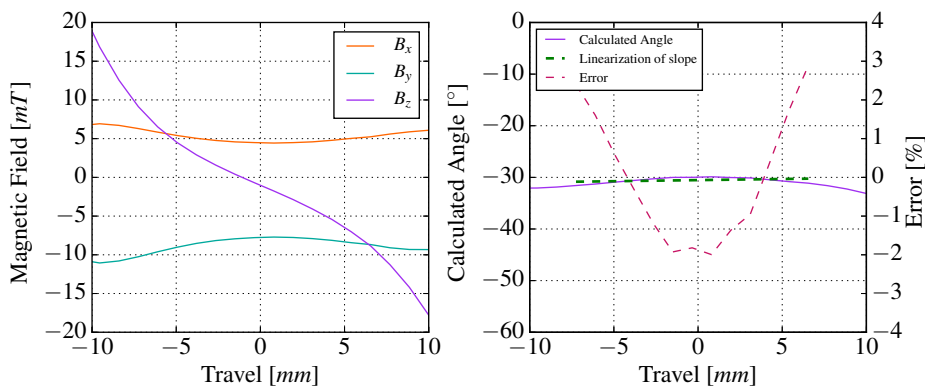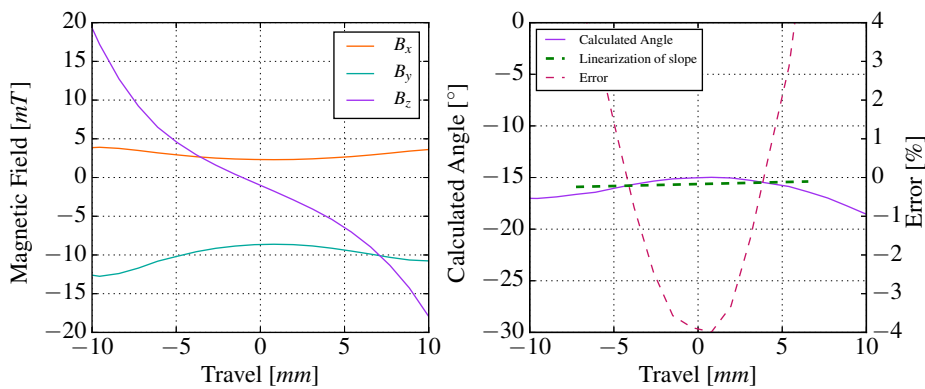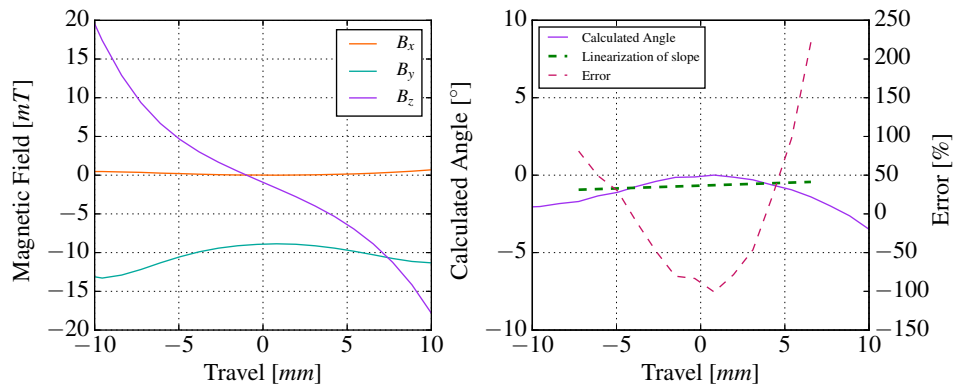
Figure D.4 – Magnetic fields B_x, B_y, B_z and the linear position calculation for $\beta = 0°$
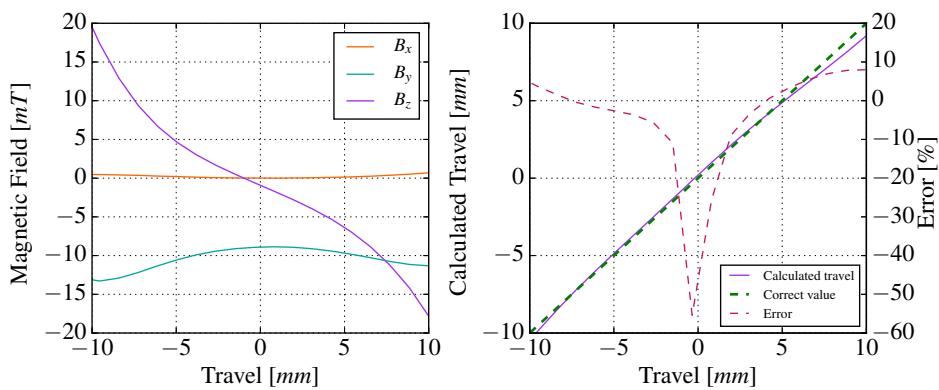
Source: Author, 2016

Figure D.5 – Magnetic fields B_x, B_y, B_z and the linear position calculation for $\beta = 15°$
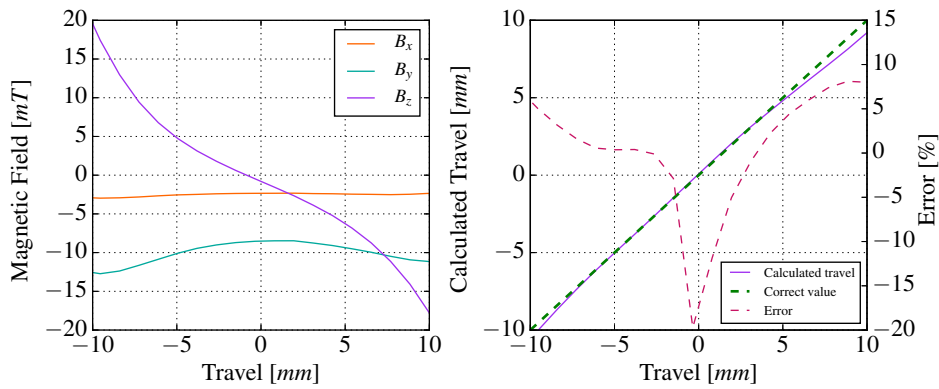
Source: Author, 2016

Figure D.6 – Magnetic fields B_x, B_y, B_z and the linear position calculation for $\beta = 30°$
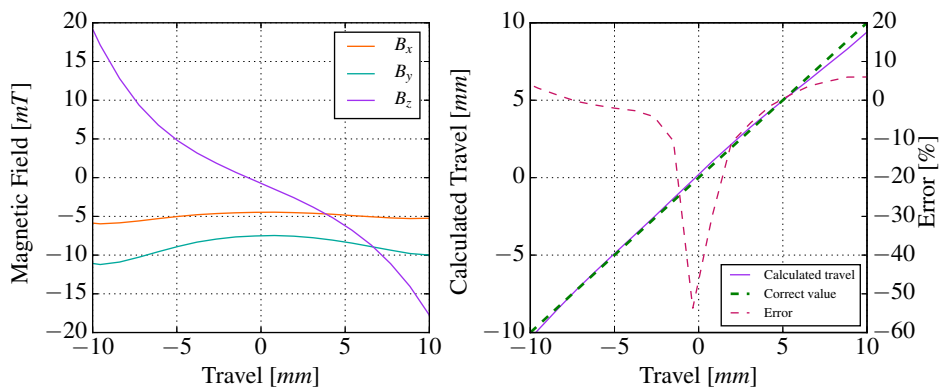
Source: Author, 2016

Figure D.7 – Magnetic fields B_x, B_y, B_z and the linear position calculation for $\beta = 45°$

Source: Author, 2016

D.2 Angular position calculation

Figure D.8 – Magnetic fields B_x, B_y, B_z and the angular position calculation for $\beta = -45°$

Source: Author, 2016

Figure D.9 – Magnetic fields B_x, B_y, B_z and the angular position calculation for $\beta = -30°$
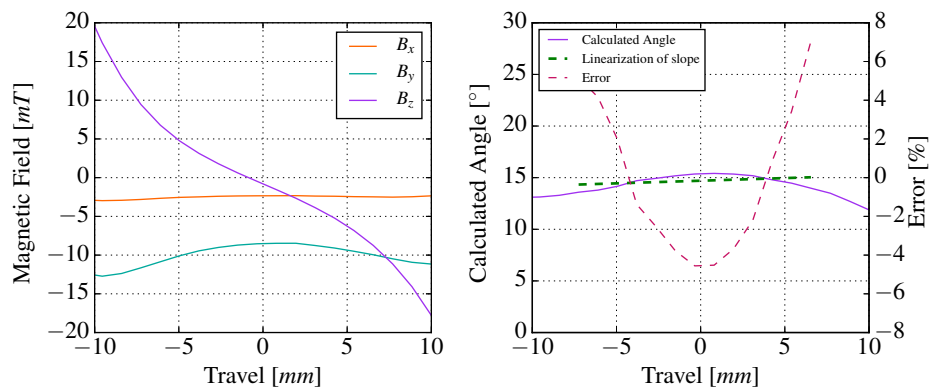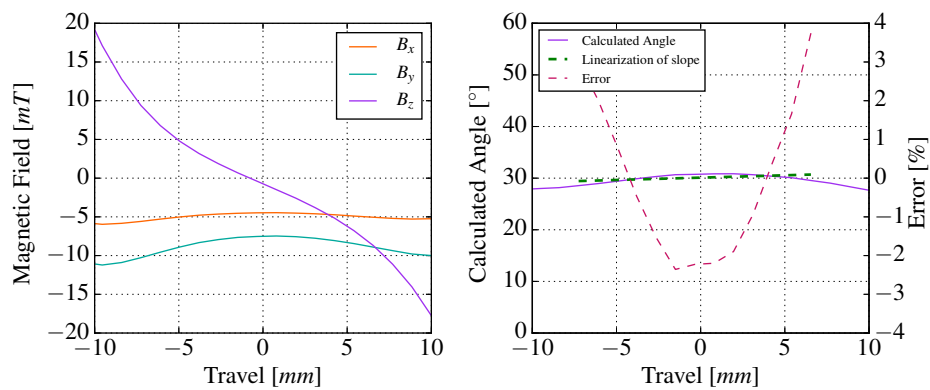

Source: Author, 2016

Figure D.10 – Magnetic fields B_x, B_y, B_z and the angular position calculation for $\beta = -15°$

Source: Author, 2016

Figure D.11 – Magnetic fields B_x, B_y, B_z and the angular position calculation for $\beta = 0°$
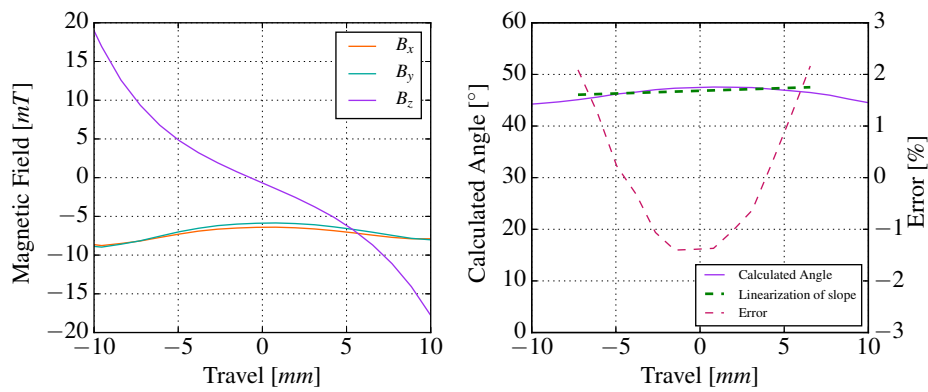

Source: Author, 2016

Figure D.12 – Magnetic fields B_x, B_y, B_z and the angular position calculation for $\beta = 15°$

Source: Author, 2016

Figure D.13 – Magnetic fields B_x, B_y, B_z and the angular position calculation for $\beta = 30°$

Source: Author, 2016

Figure D.14 – Magnetic fields B_x, B_y, B_z and the angular position calculation for $\beta = 45°$

Source: Author, 2016

## APPENDIX E – RESULTS OF THE ROAD PROFILE CALCULATION

This appendix presents the results for the linear position calculation in comparison to a randomly generated road profile. As stated in chapter 6, the d range in this results is from $-10\,mm$ to $10\,mm$. The results will be presented in two sections, where the first shows the linear position calculation results using the Equation 19 in seven scenarios, *i.e.*, $\beta = [-45, -30, -15, 0, 15, 30, 45]°$ and the second section shows the linear position detection using the lookup table method.
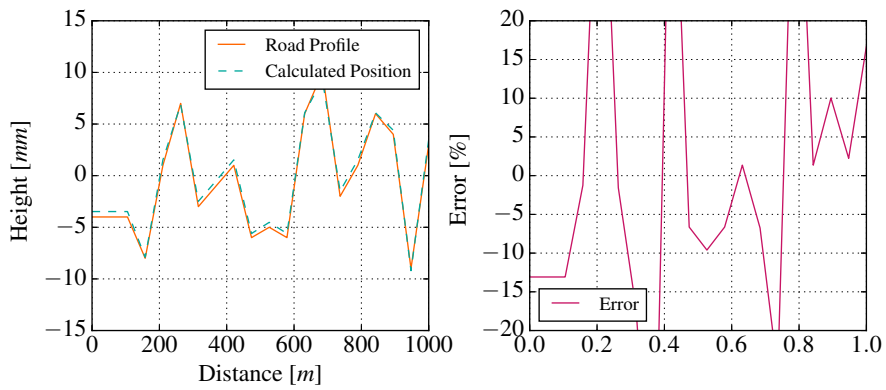
E.1 Linear position calculation

Figure E.1 – Linear position calculation for $\beta = -45°$
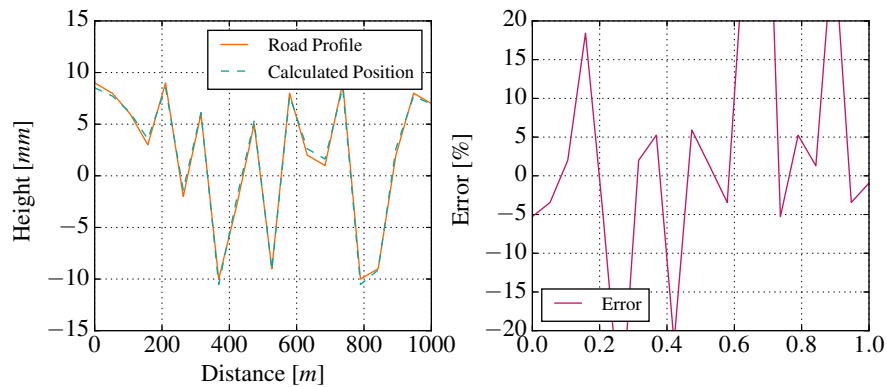
Source: Author, 2016

Figure E.2 – Linear position calculation for $\beta = -30°$
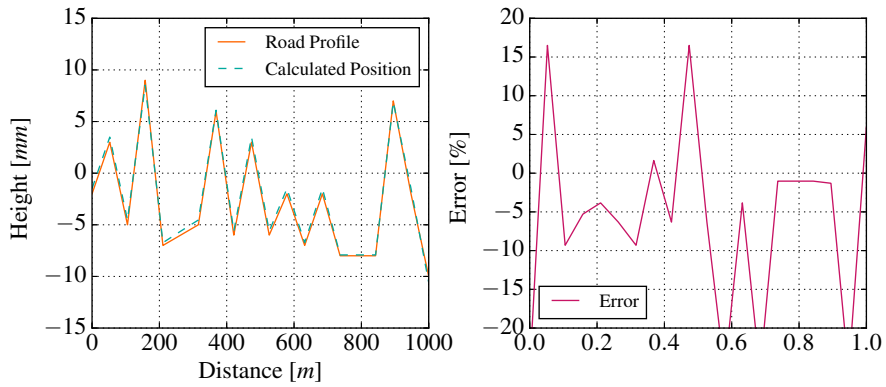
Source: Author, 2016

Figure E.3 – Linear position calculation for $\beta = -15°$

Source: Author, 2016

Figure E.4 – Linear position calculation for $\beta = 0°$

Source: Author, 2016

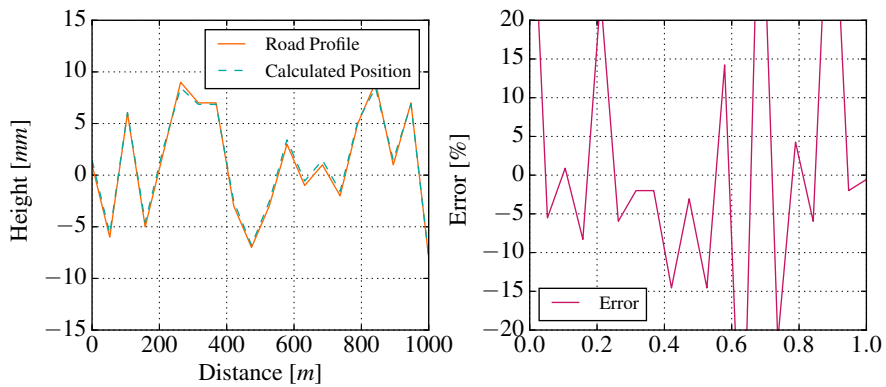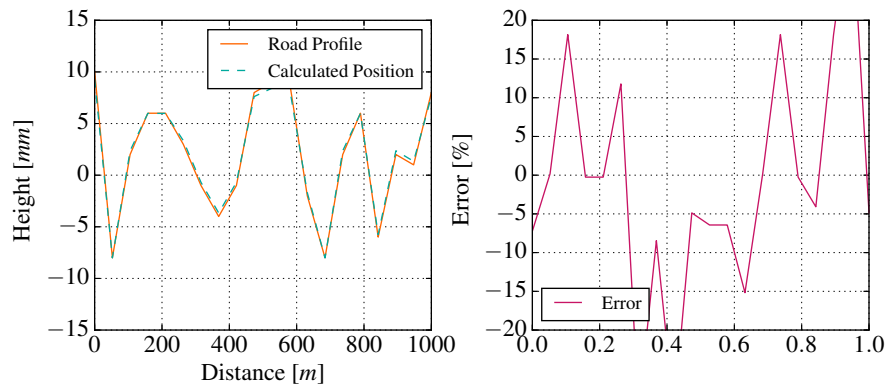Figure E.5 – Linear position calculation for $\beta = 15°$

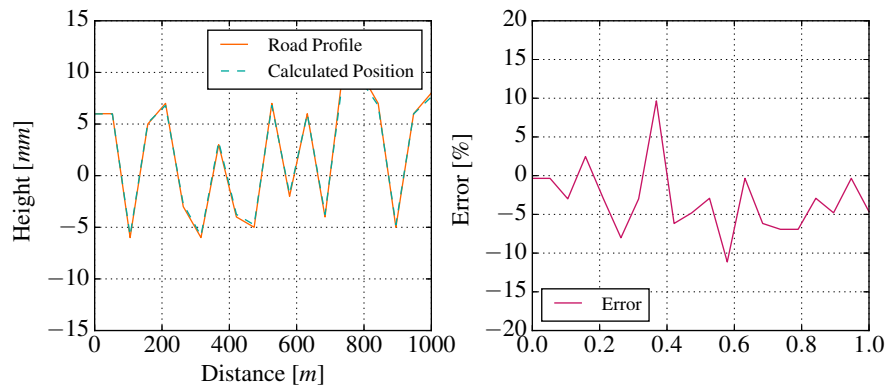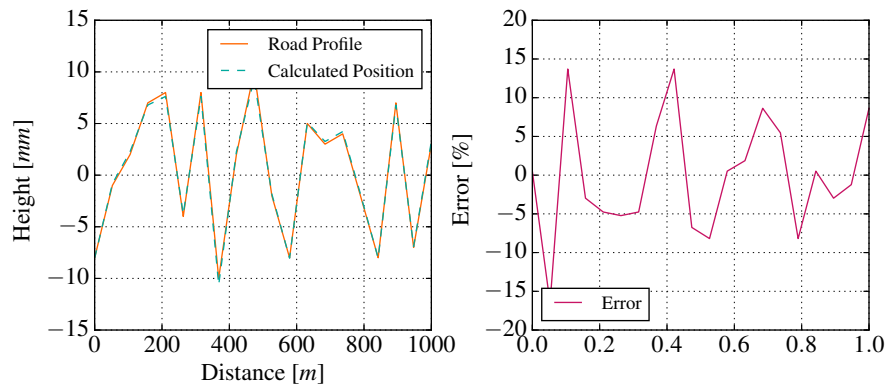Source: Author, 2016

Figure E.6 – Linear position calculation for $\beta = 30°$

Source: Author, 2016

Figure E.7 – Linear position calculation for $\beta = 45°$

Source: Author, 2016

Annex

ANNEX A – ROBOT SPECIFICATION TABLE

This annex presents the specification table of the robot used on the experiments. (3D Systems, 2016).

2.4 Spezifikationen

Element		E2C251*	E2C351*
Armlänge	1. & 2. Arm	125 mm / 125 mm	225 mm / 125 mm
Gewicht (das Gewicht der Kabel ausgenommen)		E2C**1S, C: 14 kg / E2C**1SM, CM: 16 kg	
Antriebsmethode	Alle Achsen	AC Servomotor	
Max. Geschwindigkeit *1	1. & 2. Achse	2900 mm/s	3600 mm/s
	3. Achse	1100 mm/s	
	4. Achse	2600 Grad/s	
Wiedergenauigkeit	1. & 2. Achse	± 0.008 mm	± 0.010 mm
	3. Achse	± 0.010 mm	
	4. Achse	± 0.015 Grad	
Max. Arbeitsbereich *2	1. Achse	± 90 Grad	± 110 Grad
	2. Achse	± 135 Grad	± 145 Grad
	3. Achse	E2C**1S, SM 120 mm / E2C**1C, CM: 100 mm	
	4. Achse	± 360 Grad	
Max. Pulsebereich	1. Achse	0 bis +163840	-18205 bis +182045
	2. Achse	± 76800	± 82489
	3. Achse	E2C**1S, SM: -36864 bis 0 / E2C**1C, CM: -30720 bis 0	
	4. Achse	± 46695	
Auflösung	1. Achse	0.0010986 Grad/Pulse	
	2. Achse	0.0017578 Grad/Pulse	
	3. Achse	0.0032552 mm/Pulse	
	4. Achse	0.0077097 Grad/Pulse	
Motorstromverbrauch	1. Achse	150 W	
	2. Achse	150 W	
	3. Achse	150 W	
	4. Achse	150 W	
Nutzlast	Nominal / max.	1 kg / 3 kg	
4. Achse erlaubtes Trägheitsmoment *3	Nominal / max.	$0.005 \ kg \cdot m^2$ / $0.050 \ kg \cdot m^2$	
Schaftdurchmesser / Durchgangsbohrung		$\phi \phi 16$ (h7) mm / ϕ 11 mm	
3. Achse Abwärts-Kraft		150 N	
Anwenderverkabelung Elektrisch		15 Adrig (15-Pin D-Sub Anschluss)	
Anwenderverkabelung Pneumatik		2 Pneumatikschläuche (ϕ 6 mm), 1 Pneumatikschlauch (ϕ 4 mm) Zulässiger Druck: 0.59 MPa (6 kgf/cm²)	
Umgebungsbedingungen	Umgebungstemperatur	5 bis 40°C (mit minimaler Temperaturschwankung)	
	Relative Luftfeuchtigkeit	10 bis 80% (keine Kondensation)	
Equivalenter ununterbrochener A-gewichteter Schalldruckpegel *4gel)		LAeq = 66.3 dB (A) oder darunter	
Verwendbare Steuerungen		RC520 / RC420	
Vorgabewerte	SPEED	5	
	ACCEL	10,10	
	SPEEDS	50	
	ACCELS	200	
	FINE	10,10,10,10	
	WEIGHT	1,125	
Reinraum-Modell	Reinlichkeits-Grad	Reinheitsklasse: 10 oder entsprechend Staubmenge: 10 Partikel oder weniger (0.13μm Durchmesser oder größer) (In 28317cm³ (1cft) Probeluft um den Mittelpunkt des Arbeitsbereiches herum)	
	Abluftsystem *5 — Abluftschlauch	Polyurethan-Schlauch Außendurchmesser ϕ 8 mm	
	Abluftsystem *5 — Empfohlene Abluft-Durchflussmenge	Etwa 1000 cm³/s (Normal)	

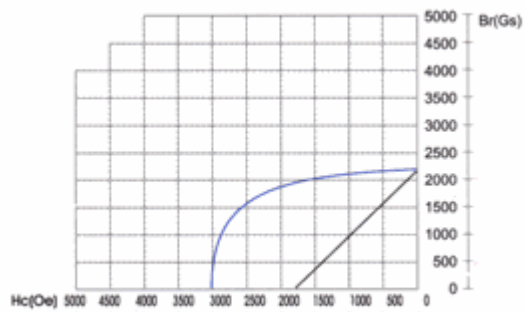# ANNEX B – MAGNET SPECIFICATION TABLE

This annex presents the specification table of the magnet used on the experiments. (ChenYang Technologies GmbH, 2006).

# Magnetic Properties of Hard Ferrite (Ceramic) Magnets

Material	Remanence		Coercivity		Intrinsic Coercivity		Max. Energy Product	
	Br (mT)	Br (kGs)	bHc (kA/m)	bHc (kOe)	iHc (kA/m)	iHc (kOe)	(BH)max (KJ/m^3)	(BH)max (MGOe)
Y10	200-235	2.00-2.35	125-160	1.57-2.01	210-280	2.64-3.52	6.5-9.5	0.8-1.2
Y10T	>200	>2.00	128-160	1.60-2.00	128-160	1.60-2.00	6.4-9.6	0.8-1.2
Y20	320-380	3.20-3.80	135-190	1.70-2.38	140-195	1.76-2.45	18.0-22.0	2.3-2.8
Y22H	310-360	3.10-3.60	220-250	2.77-3.14	280-320	3.52-4.02	20.0-24.0	2.5-3.0
Y23	320-370	3.20-3.70	170-190	2.14-2.38	190-230	2.39-2.89	20.0-25.5	2.5-3.2
Y25	360-400	3.60-4.00	135-170	1.70-2.14	140-200	1.76-2.51	22.5-28.0	2.8-3.5
Y25BH	360-390	3.60-3.90	176-216	2.20-2.70	215-231	2.70-2.90	23.9-27.1	3.0-3.4
Y26H	360-390	3.60-3.90	220-250	2.77-3.14	225-255	2.83-3.21	23.0-28.0	2.9-3.5
Y27H	370-400	3.70-4.00	205-250	2.58-3.14	210-255	2.64-3.21	25.0-29.0	3.1-3.7
Y28	370-400	3.70-4.00	175-210	2.20-2.64	180-220	2.26-2.77	26.0-30.0	3.3-3.8
Y30	385-405	3.85-4.05	176-224	2.20-2.80	184-226	2.30-2.84	27.5-30.5	3.45-3.95
Y30BH	380-400	3.80-4.00	230-275	2.89-3.46	235-290	2.95-3.65	27.0-32.5	3.4-4.1
Y32	400-420	4.00-4.20	160-190	2.01-2.38	165-195	2.07-2.45	30.0-33.5	3.8-4.2
Y33	410-430	4.10-4.30	220-250	2.77-3.14	225-255	2.83-3.21	31.5-35.0	4.0-4.4
Y35	400-420	4.00-4.20	160-190	2.01-2.38	165-195	2.07-2.45	30.0-33.5	3.8-4.2
Y35H1	395-415	3.95-4.15	251-259	3.15-3.25	255-271	3.20-3.40	29.6-32.8	3.7-4.1
Y35H2	390-410	3.90-4.10	236-295	3.30-3.70	275-299	3.45-3.75	28.8-32.0	3.6-4.04
Y35H3	405-425	4.05-4.25	223-247	2.80-3.10	231-255	2.90-3.20	30.2-35.4	3.8-4.4
Y35H-4H	370-390	3.70-3.90	270-302	3.40-3.80	326-358	4.10-4.50	25.6-28.8	3.2-3.6
Y38B	410-430	4.10-4.30	251-275	3.15-3.45	255-279	3.20-3.50	31.8-35.0	4.0-4.4
Y38H	395-415	3.95-4.15	287-309	3.60-3.90	311-333	3.90-4.20	29.5-32.7	3.7-4.1
Y40E	370-390	3.70-3.90	279-301	3.50-3.80	382-414	4.80-5.20	25.6-29.4	3.2-3.6
Y40B	410-430	4.10-4.30	290-324	3.65-3.95	307-329	3.85-4.15	32.6-34.4	4.0-4.4
Y45E	420-440	4.20-4.40	318-342	4.00-4.30	386-410	4.85-5.15	33.5-36.5	4.2-4.6
Y45B	430-450	4.30-4.50	247-271	3.10-3.40	251-275	3.15-3.45	35.1-38.3	4.4-4.8

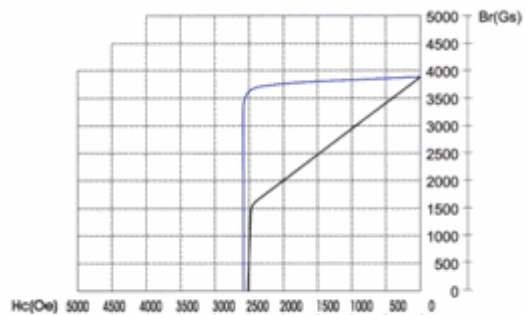# Typical Demagnetization Curves of Ceramic Magnets (Hard Ferrite)
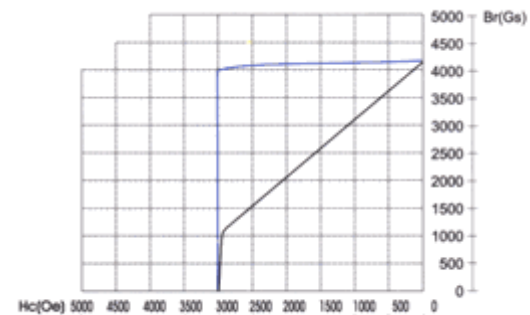
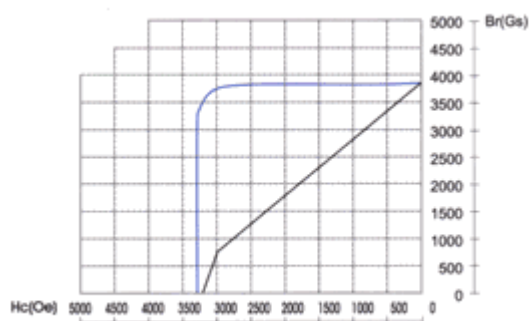| Y10 Isotropic Ferrite Grade	Y25 Anisotropic Ferrite Grade
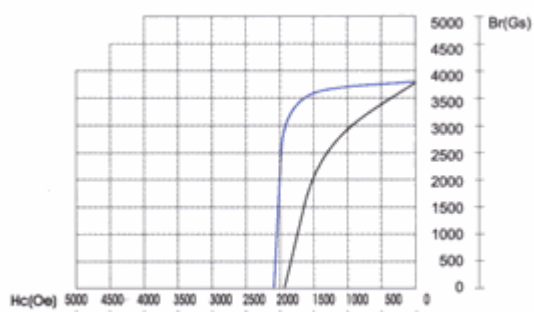
Y30 Anisotropic Ferrite Grade	Y33 Anisotropic Ferrite Grade

Y30BH Anisotropic Ferrite Grade	Y35 Anisotropic Ferrite Grade